Final Report

Root Cause Analysis of the MP 171 Fort Ransom Keystone Pipeline Rupture

Prepared for:
South Bow

Purpose:
Report on the root causes leading to the MP 171 Fort Ransom Keystone pipeline rupture.

BLADE ENERGY PARTNERS

2600 Network Boulevard, Suite 550
Frisco, Texas 75034

1-800-849-1545 (toll free)
+1 972-712-8407 (phone)
+1 972-712-8408 (fax)

16285 Park Ten Place, Suite 600
Houston, Texas 77084

1-800-319-2940 (toll free)
+1 281-206-2000 (phone)
+1 281-206-2005 (fax)

ISO 9001:2015 Certified
www.blade-energy.com

Date:
September 15, 2025

Version:
0

Project Number:
SOB-25-003

Version Record

Version	Issue Date	Issued As/ Type of Version	Author	Checked By	Project Leader
0	September 15, 2025	Final	RM/JS/KG/RK/BM/PC	RK/RM/JS/KG	RK

Version History

Version	Date	Description of Change

Table of Contents

List of Figures

List of Tables

1 Executive Summary

The South Bow Keystone Pipeline is a hazardous liquid pipeline system with assets in Canada, the US Midwest, and the Gulf Coast. In the US, the assets formerly known as Phase 1 Keystone pipeline consist of 1,086 miles of 30-inch-diameter X70 pipe, constructed between May 2008 and March 2010. The KS6 pipeline segment, spanning from the Fort Ransom pump station to the Freeman pump station, traverses the states of North Dakota and South Dakota, and is the subject of this root cause analysis (RCA) report.

There was a rupture on April 8th, 2025, 1,648 ft downstream of the Fort Ransom pump station in the KS6 segment. The MP 171 rupture occurred when the pressure on the line increased to 1,252 pounds per square inch (psi). The maximum operating pressure (MOP) is 1,440 psi (80% SMYS). A similar rupture occurred in October 2019 in the KS5 segment, 585 ft downstream of the Edinburg pump station. Both failures occurred due to a subcritical crack that initiated and grew from an ID weld toe of the double-submerged arc-welded (DSAW) seam in the pipe. Both failures occurred in pipe sections manufactured by Berg Pipe.

The KS6 pipeline segment was constructed in 2009 and began operations in 2010. The pipeline ruptured due to a subcritical crack reaching critical depth in the heat-affected zone (HAZ). The growing crack went undetected during multiple crack in-line inspection (ILI) runs. The pipeline has undergone approximately 546 equivalent MOP-to-ambient pressure cycles over the last 15 years, which is generally inadequate to initiate a crack and then propagate to failure.

Fatigue failure occurs in two steps: crack initiation, followed by propagation to a critical crack size, and finally, failure. The weld in question had a peaking (roof topping or angular misalignment) angle of approximately 12 to 16 degrees, and a weld bead offset. The weld was modeled using finite element analysis (FEA), which provided a stress concentration factor (SCF) under pressure loading and strain to estimate the number of cycles to crack initiation. Using the Smith-Watson-Topper model, it was estimated that the weld toe region would require anywhere from 130 to 478 ambient to MOP cycles to initiate a crack. The 546 MOP cycles from 2010 to 2025 are insufficient to initiate and propagate a crack to failure.

A fracture mechanics-based fatigue crack growth rate (FCGR) analysis was conducted to assess crack propagation. FCGR analysis requires an initial crack size. The initial crack size in 2010, when it was placed into operation, would have had an approximate depth of 12% of wall thickness to have grown to critical size (failure) in 2025 following 546 MOP cycles.

A more detailed examination revealed that the entire failure was due to fatigue (with possible enhanced growth rates by environment and microstructure). A scanning electron microscope (SEM) examination revealed two distinct fracture surface regions. Closer to the ID, the fatigue striations were characteristic of fatigue in air. The fractographic data indicate a period during which fatigue may have occurred in air (ID to around 10% wall thickness). In contrast, there was a period during which hydrogen and microstructure played a role in the fatigue process (10% to 78% wall thickness), as demonstrated by increased brittleness.

Using a LECO (Laboratory Equipment Corporation) ONH836 test instrument according to the inert gas fusion (IGF) method, we found slightly increased total hydrogen levels in the weld, HAZ, and base metal of the pipe used to transport the oil, compared to the unused Berg pipe in the yard. Furthermore, XPS analyses of the scale intimate with the fracture surface revealed the presence of Iron sulfide and Iron sulfate, suggesting an electrochemical hydrogen uptake mechanism local to the crack tip. Finally, modeling of the high TAN bitumen (oil) along with 0.2% water showed the possibility of 18 ppm H2S within the water phase. The modeling and data demonstrate the presence of hydrogen in the pipe, which contributed to the brittleness of the HAZ, resulting in enhanced fatigue crack propagation.

The integration of fatigue modeling and fractographic data indicates that a pre-existing crack was present when the pipe commenced operations in 2010. The only plausible explanation for the pre-existing crack was that it initiated and propagated during transportation. The pre-existing crack then grew in a hydrogen environment, after crude oil transportation began in 2010, to a critical size, resulting in a pipeline rupture.

Berg had followed the relevant transit guidelines. Despite the weld geometry meeting all the API 5L guidelines in 2008, it exhibited a high stress concentration factor due to the peaking and the offset of the weld bead. This, in turn, resulted in a crack initiating and growing at the inside weld toe in the HAZ during transportation. The weld geometry at MP 171 is a primary contributor to failure.

Following the Edinburg rupture in 2019, South Bow pursued an aggressive crack in-line inspection (ILI) program utilizing ultrasonic (UT) shear wave technology. In addition to a tool verification run, South Bow conducted two ILI inspections in 2020. Despite exhibiting a probability of detection (POD) of approximately 100% in the verification runs, the two UT shear wave tools failed to detect any crack-like signal at the rupture location in 2020. The lack of detection by ILI technologies is another contributing factor to the failure.

Integrating all the detailed data review, laboratory analysis, modeling, interviews, and discussions, the Blade team utilized the Apollo RCA process to identify root causes and mitigation options. These are summarized in the table below.

Root Causes	Solutions
Seam Weld – A Combination of Peaking and Weld Bead Offset (Section	Enhanced pipe manufacturing standards and QA/QC to prevent welds with geometric anomalies.
Specifications are inadequate to locate weld peaking and weld bead offset.	
Successful verification runs that resulted in misplaced confidence in the UT shear wave technology.	Create a verification spool that features peaking welds, bead offsets, and tilted fatigue cracks.
The inability of multiple UT shear wave tools to detect this anomaly.	• Since POD is low for the current crack ILI technologies, locate, verify, and mitigate all crack-like signals. • Phased array ILI technology requires evaluation for crack detection. • A combination of ILI technologies, such as UT Compression wave, along with other factors such as pressure and cyclic loads, is used to identify peaking welds. • Assess magnetic technologies to evaluate their ability to detect cracks and also perhaps geometric anomalies in welds. • If none of the above tools exhibit efficacy, consider hydrostatic testing as an alternative. Such a test is fraught with issues, including the initiation of cracks at weld toes and the exacerbation of subcritical cracks.

Root Causes	Solutions
Crack initiated and propagated during transit.	Enhanced QA/QC and pipe manufacturing standards to prevent weld peaking and bead offset.
Crack propagation during oil transportation was further enhanced by hydrogen and HAZ microstructure.	HAZ microstructure characterization, followed by crack initiation and propagation behavior characterization in a hydrogen environment, to establish a re-inspection frequency.
The internal oil environment contributed hydrogen and cyclic pressure loads.	South Bow has already minimized cyclic loads, and this is an operational reality.

2 Background

The South Bow Keystone Pipeline is a hazardous liquid pipeline system with assets in Canada, the US Midwest, and the Gulf Coast. In the US, those assets formerly known as Phase 1 of TC Oil Pipeline Operations, Inc.'s (TC Oil) Keystone pipeline consist of 1,086 miles of 30-inch diameter pipe constructed between May 2008 and March 2010. South Bow became the designated operator of the pipeline on March 22, 2024. Phase 1 runs from the US-Canadian border at Cavalier County, North Dakota, through the states of South Dakota, Nebraska, Kansas, and Missouri, to Wood River, Illinois. The maximum operating pressure (MOP) of the South Bow Keystone Pipeline is 1,440 pounds per square inch gauge (psig). The entire system is divided into pipeline segments that are piggable.

The KS6 pipeline segment, spanning from the Fort Ransom pump station to the Freeman pump station, traverses the states of North Dakota and South Dakota, and is the subject of this root cause analysis report. This is the portion of line highlighted in light blue in Figure 1. There was a rupture on April 8th, 2025, 1,648 ft downstream of the Fort Ransom pump station. The 30-inch-diameter pipeline was manufactured using modern, high-strength, and high-toughness X70-grade material. The pipe seam has a double submerged arc weld (DSAW) with a nominal wall thickness of 0.386 in. The external coating on the pipeline was fusion bonded epoxy (FBE).

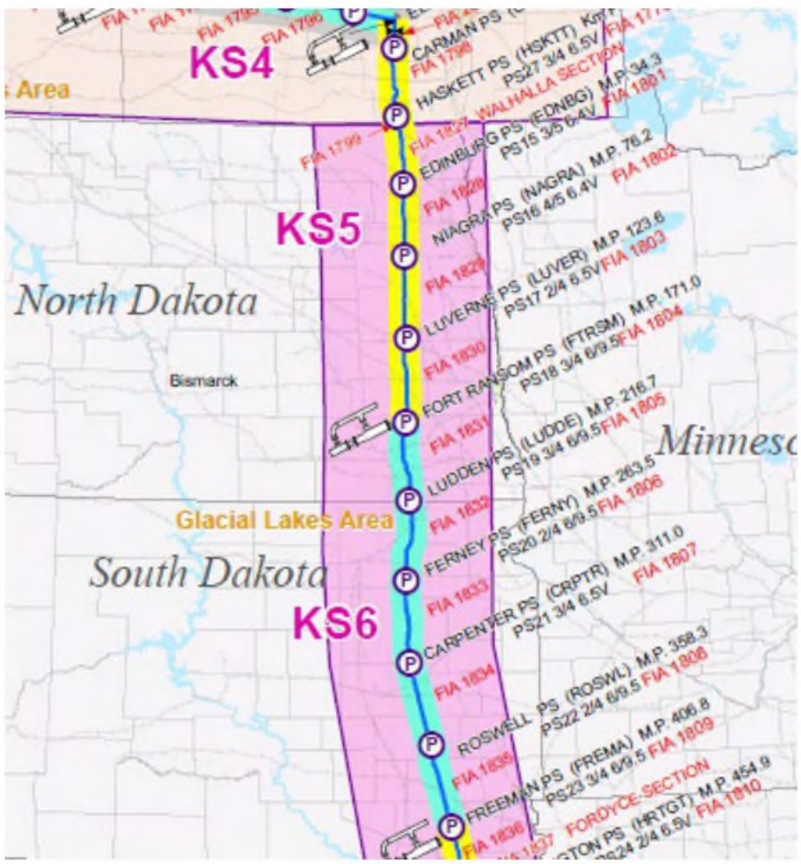

Figure 1: KS5 and KS6 Pipeline segments of the Keystone system

Berg Steel Pipe Corporation (Berg), Panama City, Florida, manufactured this pipe in 2008. Overall, 211.19 miles of Berg pipe are used in all of US Phase 1, and 42.4 miles are within the KS6 accident segment, and 134.9 miles are within all of KS6. Mittal Steel, Burns Harbor, IN, supplied the plate. TC Energy, the then operator, procured the pipe in accordance with API 5L PSL-2, 43rd edition. The pipe was manufactured in June 2008, transported by rail and truck, and arrived at the right-of-way (ROW) in July 2008. It was welded in place in August 2008. The pipeline system was hydrostatically tested in July 2009, followed by a post-construction caliper run in August 2009. The pipeline system started transporting oil products in June 2010. The pipeline maximum allowable pressure is 1,440 psi (9,929 kPa).

The MP 171 rupture along the DSAW seam occurred on April 8th, 2025, after nearly 15 years of operation, approximately 1.25 ft upstream of girth weld (GW) 610. The failure occurred at 7:42 AM CDT (5:42 MST), and the emergency shutdown was triggered at 7:43 AM CDT (5:43 MST). As part of planned maintenance, adjustments were made to system flow rates at the Fort Ransom pump station during the early morning hours of April 8th. This resulted in the station discharge pressure rising from [redacted] psi [redacted] kPa) at approximately 4:39 AM MST to a maximum of [redacted] psi [redacted] kPa) at 5:42 AM MST, when it ruptured. Following the appropriate emergency procedures and spill mitigation measures, the ruptured joint was extracted on April 13, 2025. The pipeline sample was shipped to Anderson and Associates for failure analysis. The replacement pipe joints were welded, and oil transportation through the pipeline resumed on April 14, 2025.

PHMSA issued a Corrective Action Order, CPF No. 3-2025-018-CAO (CAO), following this incident, that included various required corrective actions. These included metallurgical and mechanical testing, as well as root cause failure analysis (RCFA). The RCFA requires documenting the decision-making process and all factors contributing to the failure.

A similar incident occurred in the KS5 segment of the Keystone pipeline, 585 ft downstream of the Edinburg pump station, which ruptured in October 2019. The fish-mouth nature of the Edinburg rupture had a rupture length of [redacted] n. and a maximum rupture opening of [redacted] in., as shown in Figure 2 . Anderson conducted the failure analysis, and RSI completed a root cause analysis. Similar to the current MP 171 rupture, Berg was also the manufacturer of the 30 in. diameter X70 grade pipe that ruptured in 2019. The seam was DSAW with a nominal wall of 0.386 in. In their metallurgical failure report on the Edinburg rupture, Anderson and Associates (Anderson) concluded that there were multiple fatigue crack initiation sites, and most were coincident with small hemispherical-shaped corrosion pits at the toe of the seam weld. Furthermore, Anderson concluded that the environment did not contribute to the propagation of fatigue and fracture. The failure analysis concludes that the rupture is attributed to high-cycle fatigue cracking.

(b)(4) [redacted]

Figure 2: Edinburg rupture from the 2019 Anderson failure analysis

RSI Pipeline Solutions (RSI) conducted the RCFA of the October 2019 seam rupture incident downstream of the Edinburg pump station. The key causes (paraphrased from their 2020 RSI report) identified by RSI were as follows:

- Crack initiated at the weld, where the radial offset (high-low) did not meet the API 5L specifications, and the angular misalignment of plate edges.
- Crack initiated at pitting that was possibly caused by moisture during storage, or hydrostatic test water, or MIC at the weld toe in service. The corrosion resulted in the initiation of a fatigue crack. Furthermore, incremental crack growth analysis due to the abnormal seam geometry was a necessary condition for the fatigue failure to occur in 9.4 years. Pitting caused the initiation, and then the growth was not influenced by the pitting.
- The 2017 (b)(4) [redacted] couldn't detect this crack due to the roof-topping and radial offset affecting the probability of detection (POD).

RSI made many recommendations; a few critical ones were:

- TC Energy should continue to explore other advanced crack detection ILI technologies with improved POD for seam weld cracking
- Increase frequency and scope of mill inspections, including NDE methods to identify offset in the middle of a pipe.
- Consider a pressure cycle management program to reduce the frequency and magnitude of pressure cycles
- Control Room and Emergency Response improvements were also proposed.

Based on the Blade review, South Bow has implemented many of the recommendations by RSI. A very aggressive crack ILI program was undertaken along with verification. Further, the pressure cycles incurred through the subsequent years of operation continue to decrease. Improvements in emergency response were also noted compared to the 2019 incident.

Anderson also conducted the failure analysis of the April 8, 2025, MP 171 rupture that occurred downstream of the Fort Ransom Pump Station. The rupture itself visually has similar characteristics to the 2019 failure, as shown in Figure 3.

(b)(4) [redacted]

Figure 3: MP 171 rupture figure from the 2025 Anderson failure analysis report

There are some key conclusions in the Anderson report (paraphrased from their 2025 metallurgical report):

Fatigue initiated at ‘ratcheting markings’ along the toe of the seam weld. There were no pre-existing anomalies. There was evidence of micropitting, and some micropits acted as crack initiation sites.

- The cause of the rupture was attributed to fatigue cracking that originated along the ID toe of the seam weld.
- The fatigue crack propagation was brittle in nature. Further, a possible explanation for the brittle nature of the fatigue crack propagation is associated with the hydrogen mechanism.
- Geometric measurements of seam welds demonstrated that they were within specified limits for radial misalignment, out-of-line weld bead, and cap height per API 5L 43rd edition.

The appearance of the two failures is similar; however, the failure analysis conclusions are distinctly different. The key difference appears to be the brittle nature of the fatigue crack growth observed in the 2025 failure, compared to the presence of pure fatigue crack propagation in the 2019 failure. Additionally, unlike the Edinburg failure, the seam weld from the MP 171 failure did meet the API 5L 43rd edition specification.

3 RCFA Approach

The primary objective of a root cause analysis is to prevent all manner of pipeline integrity incidents by identifying the root and direct causes, contributing actions or conditions, and determining solutions that prevent and mitigate those causes.

The characteristics of the MP 171 seam rupture were unique. The KS6 pipeline segment was constructed between 2008 and 2009 and began operations in 2010. The pipeline ruptured due to a crack in the heat-affected zone (HAZ), which had gone undetected despite multiple crack inspection runs. The pipeline has undergone approximately 546 MOP to ambient pressure cycles over the last 15 years, and a cursory review suggests that these cycles are inadequate to initiate and grow a crack to failure. This is discussed in detail later in the report.

The overall approach taken for the root cause analysis required a detailed understanding of the mechanism of cracking, seam weld manufacturing, double jointed pipe transportation, inline inspection, fracture and fatigue analysis, metallurgical analysis, standards and procedures, Edinburg failure and RCFA, integrating all the information, and finally the Apollo RCA process to identify root causes and solutions.

The steps in the RCA process undertaken here are as follows:

1. Data Collation and Review
    a. An extensive SharePoint repository was created and populated by the South Bow team.
    b. Pipeline Data, Design, Soil, Geotechnical
    c. Pipeline Manufacturing/Construction data (Weld, Base Metal, Transportation)
    d. Failure Site Photographs, Metallurgical Data
    e. ILI Data
    f. Operations (O & M procedures, MOC, DRA, SCADA, Product Corrosiveness, CP, DCVG, CIS)
    g. Maintenance and Repairs
    h. IMP and Risk
    i. Emergency Response/Leak Detection
    j. Org Charts
    k. Edinburg Failure
    l. CAO/Restart Plan
    m. Standards/Industry Papers
2. Interview/Discussions

    There was a designated primary contact from the South Bow team, who coordinated all the data and discussion requests.

    a. South Bow: Personnel from different teams, which included LPCC, Keystone Control Center, Scheduling and Crude Quality, Pipe Integrity, and Emergency Management.
    b. Berg (Written Questions)

   c. (b)(4) [redacted]
   d. QA/QC for Berg Pipe Manufacturing and Transportation

3. Emergency Response and Leak Detection. This was analyzed using rupture event-related documents, internal standards and procedures, and interviews with key personnel.
4. Manufacturing/Construction and Transportation Process analysis. This included an assessment of the process of creating the peaking, hi-lo, and weld offset, as well as many other weld defects. Additionally, a thorough understanding of the QA/QC and transportation process was developed.
5. Inline inspection technologies that were deployed and the associated decision-making.
6. Additional Metallurgical examination to inform the RCFA included Raman Spectroscopy, XPS, Leco testing, residual stress measurements, extensive SEM examination of the fracture surface, additional J-R testing of the used and unused pipe, reviewing the weld geometry, and finally, a detailed review of the Anderson report.
7. Extensive fracture mechanics and fatigue modeling. This included FEA modeling of the seam weld and associated stress concentration factor. Fatigue crack initiation and propagation were modeled.
8. A facilitator-led root cause analysis process was conducted that integrated all of the above data and analysis to arrive at root causes.

4 Laboratory Assessment

Metallurgical analyses of the Edinburg, ND rupture [1] at MP 34.3, and the Fort Ransom, ND [2] at MP 171 were completed by Anderson and Associates, in Houston, TX. The metallurgical analysis for the MP 171 rupture identified fatigue crack initiation and growth as the primary cause of the failure. Furthermore, brittle features were observed on the fracture surface, which were attributed to hydrogen.

As part of the RCA, Blade undertook some additional metallurgical and other analyses that are discussed below.

4.1 Hydrogen Analysis

Based on fractography of the preexisting crack, Anderson and Associates reported the probability of hydrogen playing a role in the failure. Anderson reported secondary cracks consistent with HIC-type cracks [2]. Also, the morphology of the fracture surface changed from a purely mechanical fatigue mechanism to an environmentally-assisted fatigue mechanism. Fractographic analysis for an environmentally-assisted crack and for hydrogen is presented in [2] at the midwall in Anderson Figure 21 and at the tip of the preexisting crack prior to overload failure in Anderson Figure 22. Anderson's figures are reprinted here in Figure 4. Anderson makes the argument of the possibility of hydrogen in the "Discussion and Conclusion" section, p. 98 [2].

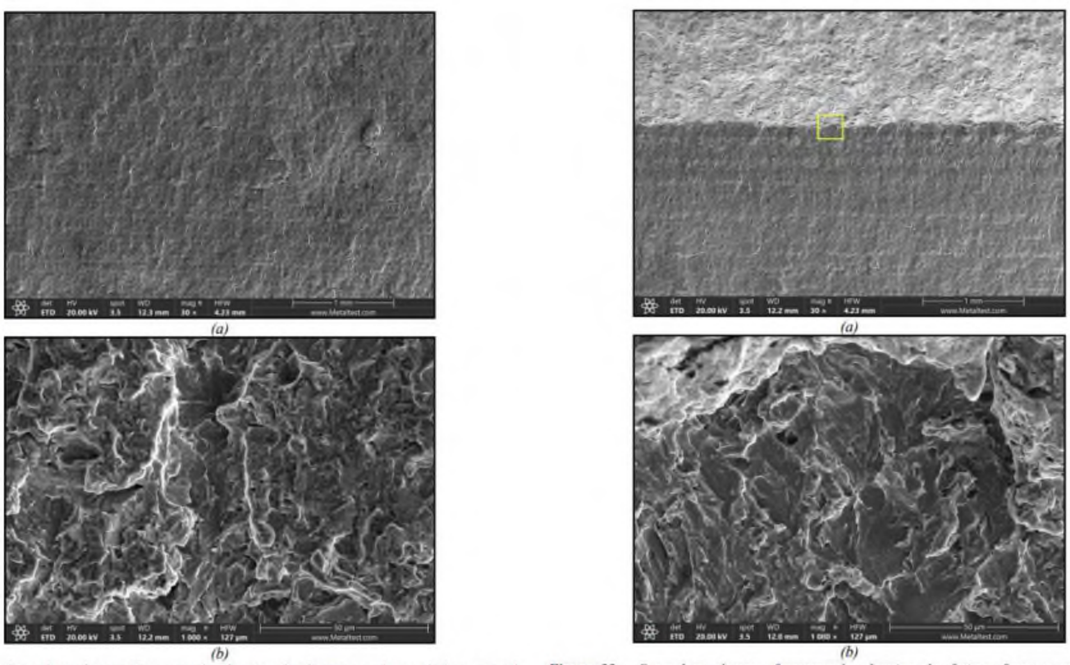

Figure 21 – Secondary electron fractographs showing the fatigue crack morphology at mid-wall. At low magnifications as shown in (a), the fracture surface was characterized as having numerous crack arrest lines oriented perpendicularly to the crack growth direction. At high magnifications (b), the fracture surface exhibited features consistent with brittle cleavage.

Figure 22 – Secondary electron fractographs showing the fatigue fracture near the final overload region (zone III). Examination of the fatigued surface at the transition zone at high magnification showed features consistent with brittle cleavage. (a) 30x (b) 1,000x.

Figure 4: Anderson images, potential hydrogen influence on fracture

Although Anderson did not observe fatigue striations, Blade did observe fatigue striations on a sample of the fracture surface supplied by Anderson, absolutely confirming fatigue as the initiation mechanism and playing a role in crack propagation. Blade also concurs with Anderson that there may be an environmentally assisted cracking mechanism accelerating the crack to failure, along with a varying microstructure through thickness—supporting evidence to be presented later in this report. For these reasons, residual bulk hydrogen was tested in samples of weld, HAZ, and base metal in the region of the failure, as well as in a D/S joint and an unused joint.

API 5L 43rd Ed. [3] and the Keystone Oil Pipeline Project Construction Contract [4] specified the use of low-hydrogen EXX18 rods with specific exposure limitations and drying procedures for tack welding. The inside and outside seam welds are track-welded, with processes and materials documented in the Berg Manufacturing Procedure Specification MPS-BNSPC-TC-03 [5]. Hydrogen in DSAW in pipelines is typically prevented rather than measured by controlling moisture in the flux per supplier recommendations, using correct heat control, and limiting hardness to less than 350 HV per API 1104 [6].

The crude oil environment with 0.5% Basic Sediment and Water (BS&W) could electrochemically create hydrogen and enhance crack propagation. To test for trapped hydrogen, samples were extracted and sent for measurement of total hydrogen content by inert gas fusion (IGF). Samples ranging from 1 g to 2 g were extracted from the subsurface material by saw cutting with flood coolant and kept on ice until analysis. Approximate locations of samples are shown in Figure 5. Each of these samples was further reduced by the test lab, resulting in two to three samples being taken at each location.

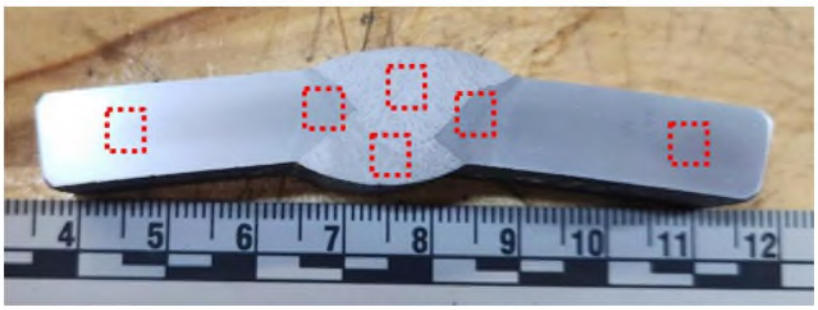

Figure 5: Example locations of hydrogen test samples

Total hydrogen results are provided, along with joint, location, and average atomic hydrogen concentrations in ppm, as shown in Table 1. Each reading is the average of two to three readings from the same location (typically triplicate). Grand average is the average total hydrogen level across the weld, HAZ, and adjacent base metal.

Table 1: Total hydrogen tests comparative results

Joint	Location	ppm w/w
GW 600 Failed Joint, At Fracture	Base Metal	1.59
	HAZ	1.72
	Weld	0.07
	Grand Average	**1.13**
GW 600 Failed Joint, Far From Fracture	Base Metal	1.33
	HAZ	1.20
	Weld	0.23
	Grand Average	**0.92**
	Base Metal	1.55

Joint	Location	ppm w/w
GW 610 Adjacent D/S Joint	HAZ	1.58
	Weld	1.04
	Grand Average	**1.39**
Unused Joint	Base Metal	0.69
	HAZ	0.44
	Weld	0.61
	Grand Average	**0.58**

The failed joint and adjacent joint returned bulk hydrogen levels higher than those of an unused joint. The precision of the LECO ONH836 tester is 0.00005mg or 0.05 w/w, so there is significant overlap; however, this finding supports the possibility of increased hydrogen in joints in service compared to unused joints.

LECO total hydrogen is a test of the average total hydrogen. Crack tip hydrogen may have been higher, but not lower. To measure crack tip hydrogen at fracture, an analysis such as secondary ion mass spectrometry (SIMS) would be necessary and performed immediately on the fracture. In this case, such a test was not possible. Further research would be necessary to determine the specific critical hydrogen level that would accelerate the FCGRs in the X70 HAZ. The RCA conclusions do not require the SIMS work.

4.2 Fractography

Anderson and Associates identified a subcritical crack in the failed seam weld prior to rupture. The crack was identified as a fatigue crack based on macroscopic observations, including the shape of the crack front, the presence of ratchet marks and possible beach marks, as well as a general brittle appearance at the microscopic level. Cracks identified as secondary cracking were cited and attributed to a possible hydrogen mechanism. The fracture surface was reanalyzed at Blade to confirm the findings and provide complementary data to the Anderson fractographic analyses.

The optical and stereo micrographs in Figure 10 show the polished and etched cross-section of the Anderson sample, identified as "Met 1", adjacent to the fracture surface. This location is directly opposite Anderson's Figures 20, 21, and 22 [2].

4.2.1 HAZ Microstructure

The cross-section is annotated with the standard DSAW HAZ zone nomenclature [7]. The schematic in Figure 6 is borrowed from Dong [7] with definitions reprinted here:

- coarse-grain heat-affected zone (CGHAZ)
- fine-grain HAZ (FGHAZ)
- intercritical HAZ (ICHAZ)
- subcritical HAZ (SCHAZ)
- unaltered CGHAZ (UA CGHAZ)
- supercritically reheated CGHAZ (SC CGHAZ)

- intercritically reheated CGHAZ (IC CGHAZ)
- subcritically reheated CGHAZ (S CGHAZ).

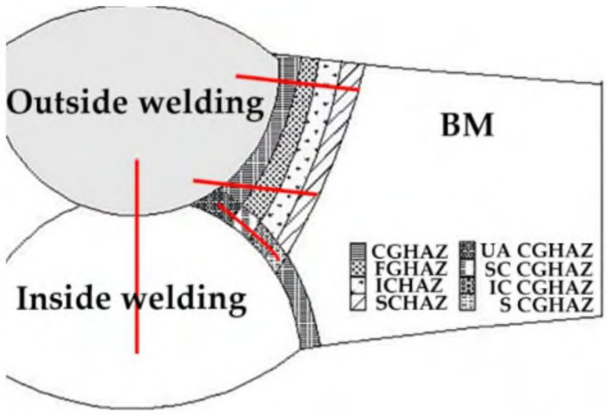

Figure 6: Schematic of DSAW weld regions borrowed from Dong

4.2.2 Overview of the Fracture Region

The overall fractography, in general, shows high-cycle fatigue in the early stages of the crack at the weld toe on the ID. Striations in this region are densely packed and occupy a large area fraction of the fracture surface in the early stages of crack growth. The morphology of the crack becomes increasingly crystallographic as it progresses through the HAZ. This is likely a combination of a changing environment and microstructure.

Figure 7 is a stereo image map of SEM image locations taken to demonstrate general changes in crack morphology and mechanism. Locations L1 and L2 depict high-cycle fatigue with fine striation spacing. These striations are consistent with fatigue in air or in a mild environment. Locations L3 and L4 show increasing area fractions of cleavage and quasi-cleavage; however, fine strations are still evident in L4. In Figure 9, Locations L5 through L8 fatigue striations are challenging to identify, as the microstructure is dominated by crystallographic fracture.

Please note that magnification was purposely varied to best present the intended features in any given region of interest. Fatigue striations require a higher magnification. Therefore, locations L1, L2, and L4 in Figure 8 are presented at 5000X. The cleavage and quasi-cleavage regions depicted in L3 in Figure 8 and L4 and L5 through L8 in Figure 9 are presented at 2500X to zoom out and demonstrate a distinct change in fracture morphology and crack advance mechanism.

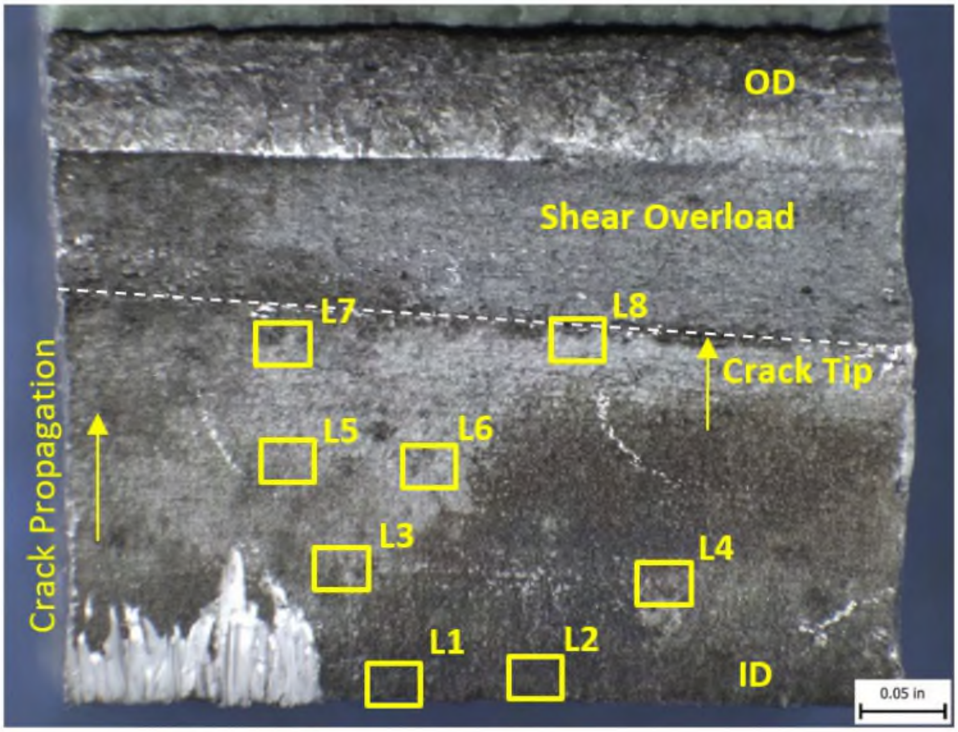

Figure 7: SEM image map from ID to OD

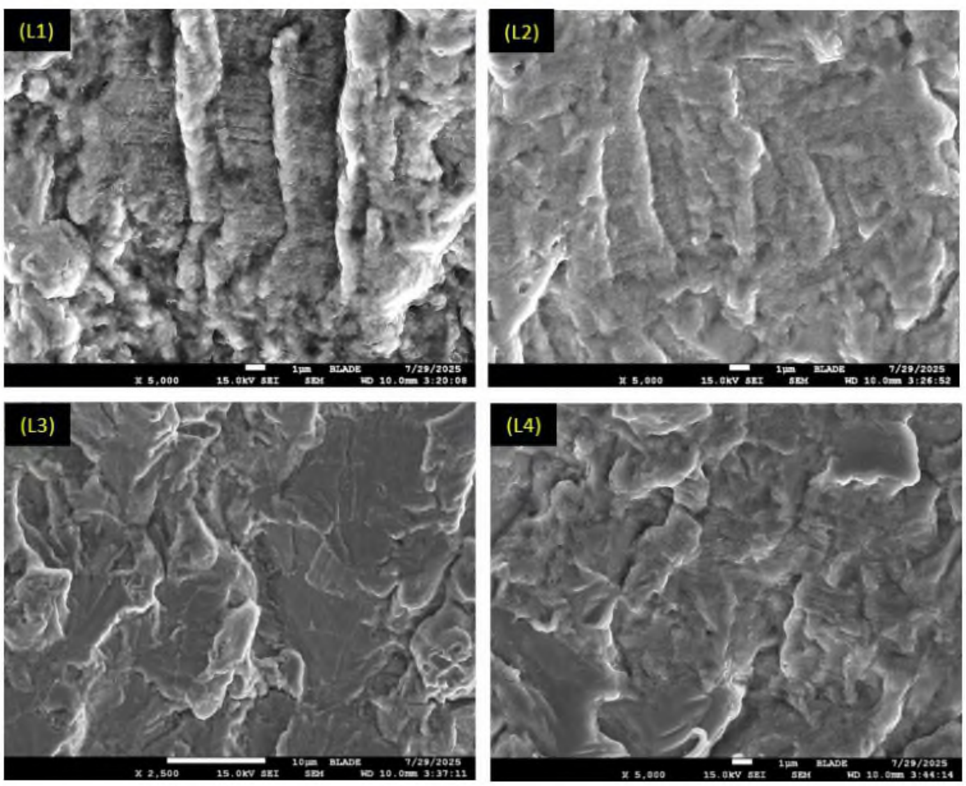

Figure 8: SEM images of locations L1 to L4, lower region of crack growth

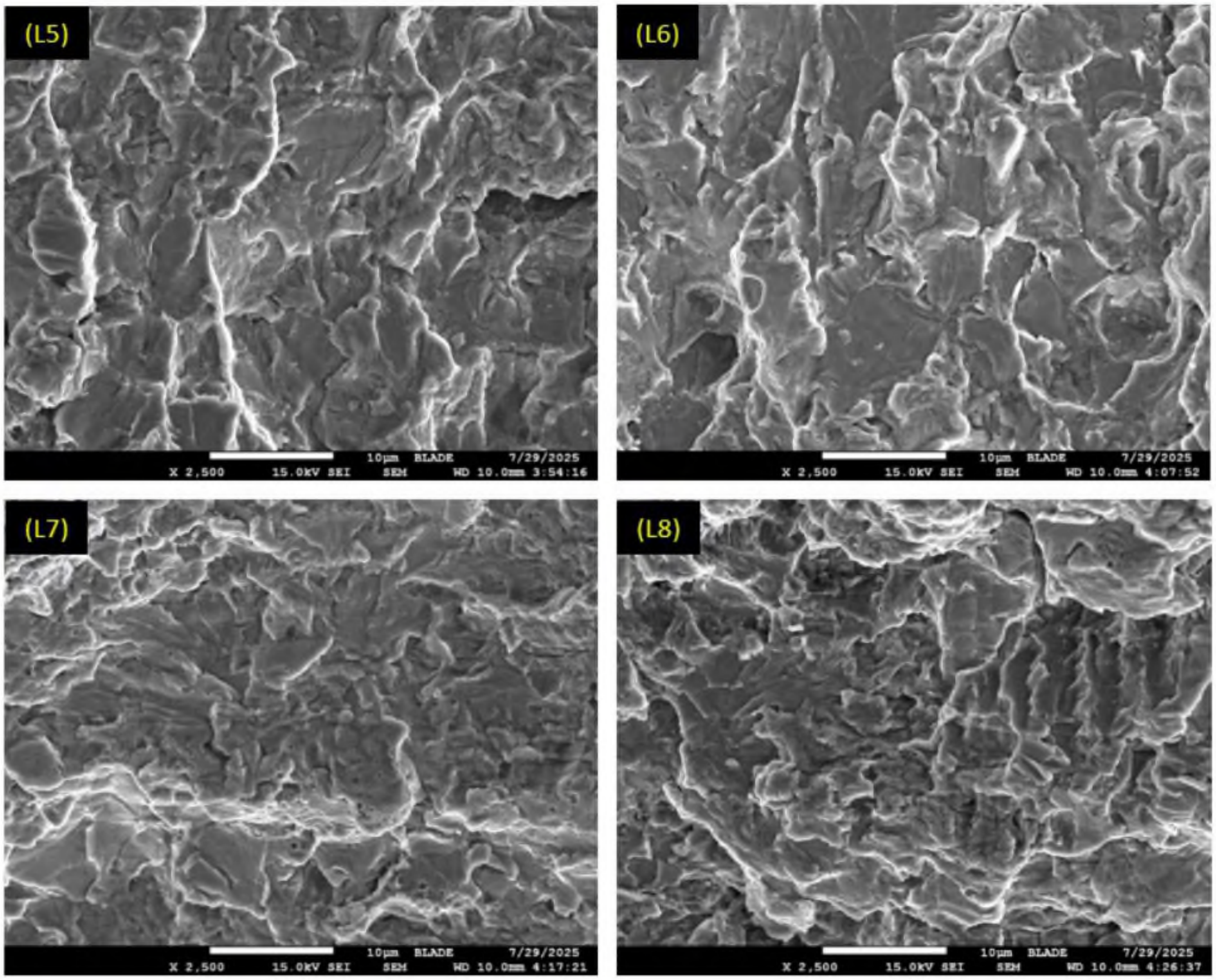

Figure 9: SEM images of locations L5 to L8, upper region of crack growth

4.2.3 Detailed Fracture Surface Assessment

Figure 10 (left) shows the fatigue crack initiated at the ID near the weld toe in the inside CGHAZ, propagated through alternating regions, reaching a critical length as it approached the outside CGHAZ. At that point, the remaining ligament failed by shear overload through the outside CGHAZ zone adjacent to the outer cap weld. This assessment is in agreement with Anderson and Associates [2]. The fractographic locations (a) through (f) are mapped on Figure 10 (right). Figure 10 (left) demonstrates the variance in grain structure and phase fractions as the crack grew from the ID to the OD. The fracture response of the material is a complex interaction of environment, stress intensity, and microstructure. Figure 11 is a map of two locations evaluated under the SEM at <10% WT near the ID.

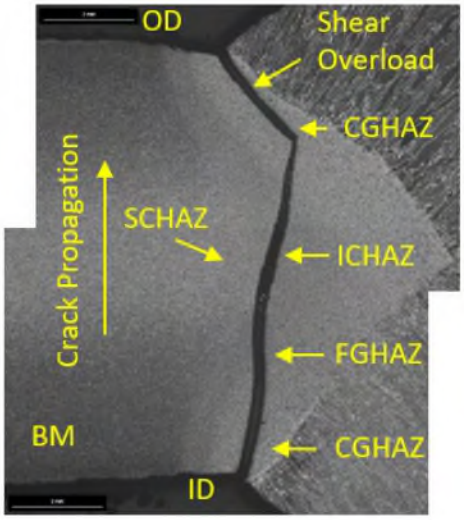

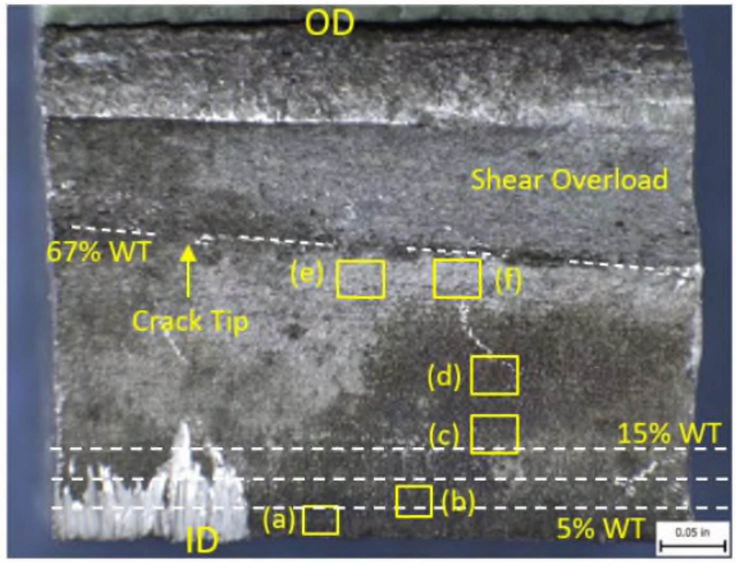

Figure 10: Optical images, cross-section, and crack face, peak depth location

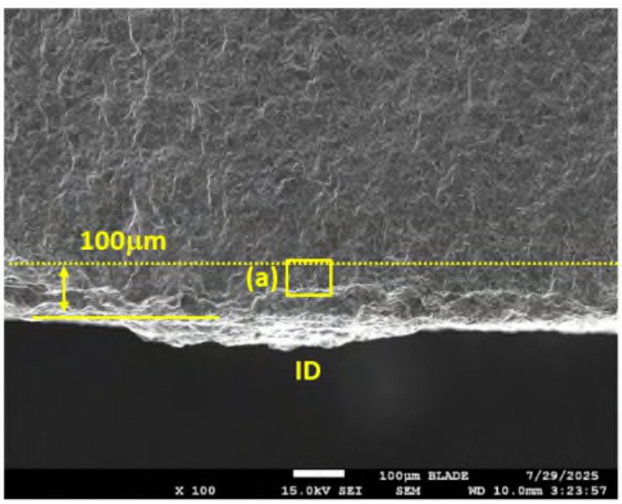

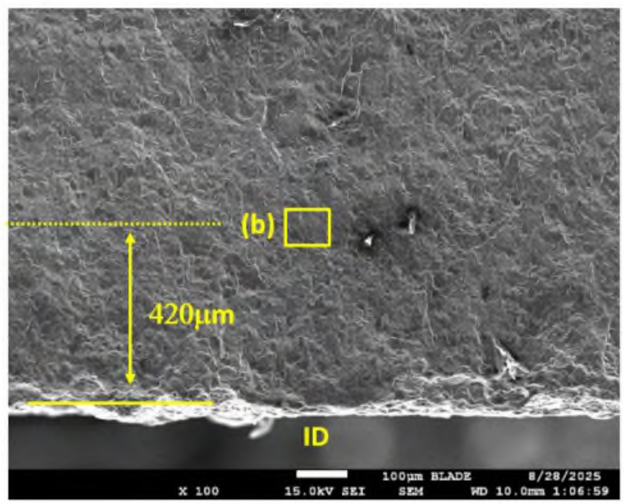

Figure 11: SEM fractograph map, fracture face, crack Initiation

Figure 12 shows the etched and polished microstructure of "Met1" at the ID near the deepest crack location. The image was taken by Anderson at 100X. At this magnification, the microstructure at locations (a) and (b) appears similar. The CGHAZ relative to both (a) and (b) appears to be non-polygonal ferrite and accicular needle-like structures of bainite.

An electron backscatter diffraction EBSD analysis would be necessary to precisely determine the phases present in the CGHAZ or any zone in the greater HAZ; however, Dong [7]. Drexler [8] et.al. describe the CGHAZ as in X70 DSAW seam welds next to the fusion line as mainly granular bainite (GB) with some bainitic ferrite (BF), polygonal/quasi-polygonal ferrite (PF), accicular ferrite (AF), and a few-percent martensite–austenite (M–A) islands along prior-austenite grain and bainite-lath boundaries. The work cited described the CGHAZ as having potentially low relative fracture toughness and lower fatigue resistance relative to the rest of the HAZ [9].

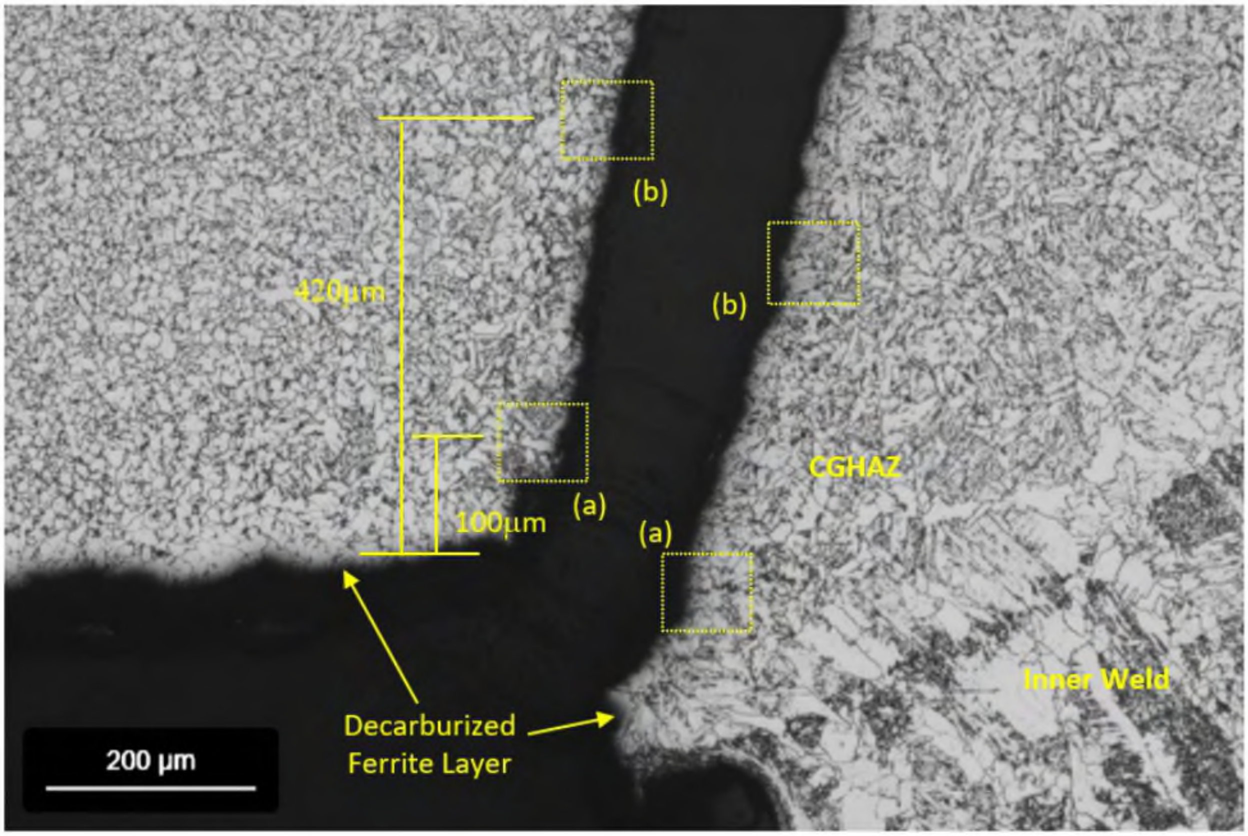

Figure 12: Anderson micrograph "Met 1" cross-section, crack initiation

Figure 13 is an SEM fractograph of location (a) at approximately 100 µm from the ID. At this specific location, fine fatigue striations dominate the area. The morphology of the striations is consistent with the scenario of forming in air and then being exposed to a mildly reactive environment, as the striations appear to be superficially pitted. According to Zhao [10] et al, fatigue striations in the CGHAZ are likely more evident in bainitic lath.

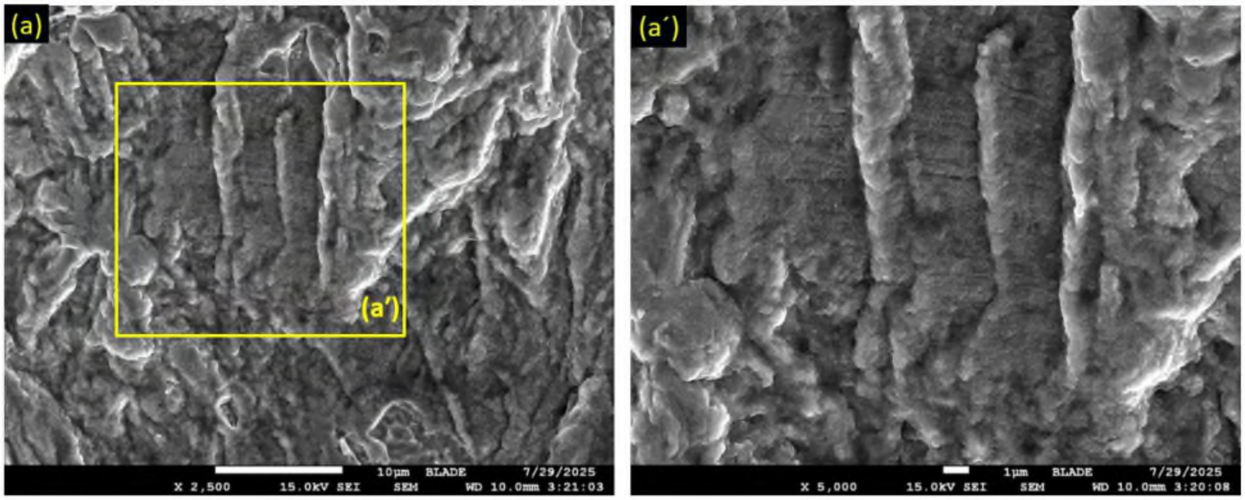

Figure 13: SEM fractography, <5% WT

Figure 14 depicts a location (b) at 420 µm of crack depth. Here, striations of similar spacing are evident. Also present are relatively large etch pits, indicating larger second-phase particles have dissolved from a non-polygonal ferrite phase over time. Etch pits occur on {100} planes in the ferrite phase [11]. Typically, this morphology indicates cleavage due to environmental interaction or improper material processing. The etch pits are formed as second-phase particles are exposed to an electrolyte and dissolved as an anode in a cathodic matrix. The cleavage would precede the dissolution, indicating that the local phase is susceptible to environmentally enhanced FCG. Hydrogen uptake from the dissolution of second-phase particles may occur. The size of the preexisting 2nd-phase particle determines the size of the etch pit. Etch pits of this size cannot be attributed to metal dissolution during sonic cleaning, given the short exposure time and low concentrations. Therefore, we know the in-situ environment was interacting with the freshly exposed metal of the crack face.

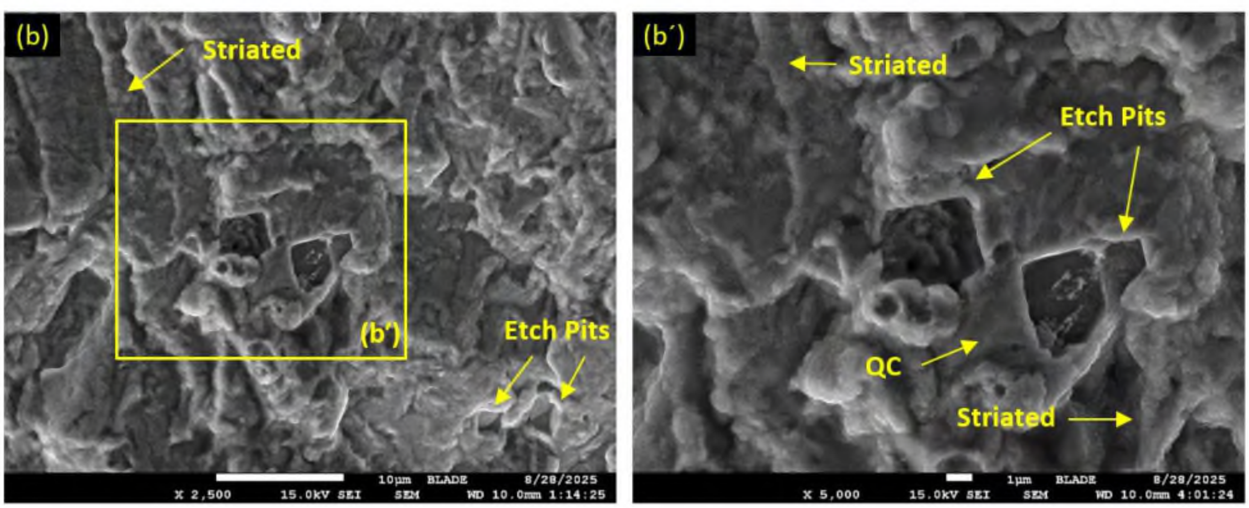

Figure 14: SEM Fractography, 10% WT

Zhao [10] suggested fatigue striations are likely most evident in lathe bainite, and this phase tends to exhibit river patterns coincident with the direction of crack propagation in the CGHAZ [10]. Note that the features exhibiting fatigue striations have an acicular shape consistent with a bainitic phase, whereas the flat or quasi-cleavage facets are consistent with non-polygonal ferrite.

SEM fractography of crack depth at 20 to 30% WT is shown Figure 15 and Figure 16, respectively. The fractography shown in these figures represents crack propagation that may enter a FGHAZ. Anderson did not take high magnification optical micrographs of this region, so a detailed optical analysis or comparison could not be made.

Location (c) Figure 15 exhibits fatigue striations on similar phase structures to Location (a) Figure 15 . However, there is a greater area fraction of quasi-cleavage (QC) crystallographic fracture. The striation spacing is slightly larger in (c) than in (a), suggesting a slight advance in radical crack growth rate. The greater area fraction of the cleaving ferrite phase may be increasing the crack growth rate by redistributing the load to the residual phases. Further research is required to confirm this assertion. Figure 15 appears to show the onset of different fracture mechanisms in addition to cleavage. Figure 18 maps the two locations evaluated by SEM near the crack tip.

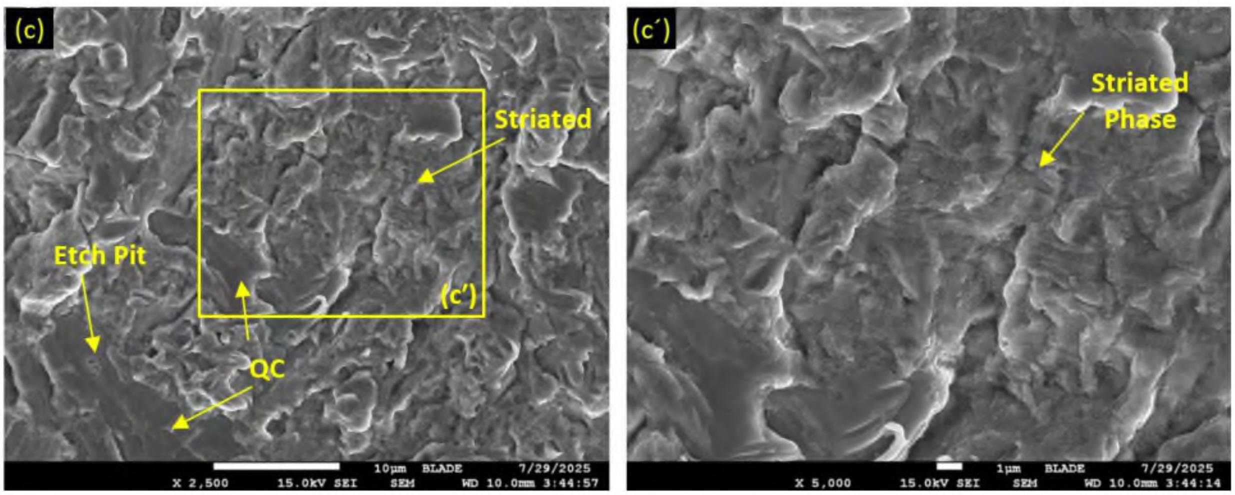

Figure 15: SEM fractography, 20% WT

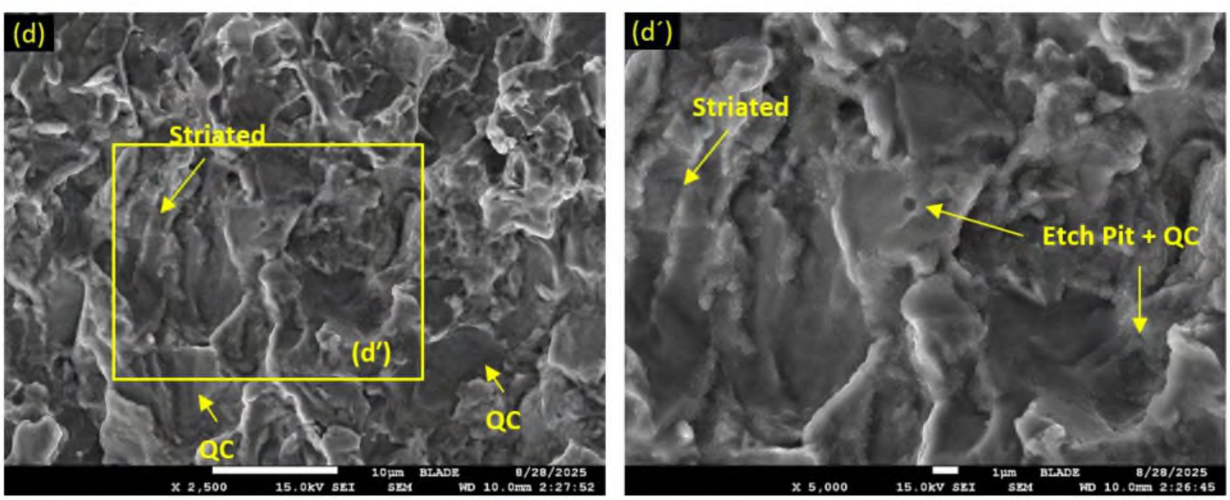

Figure 16: SEM fractography, 30% WT

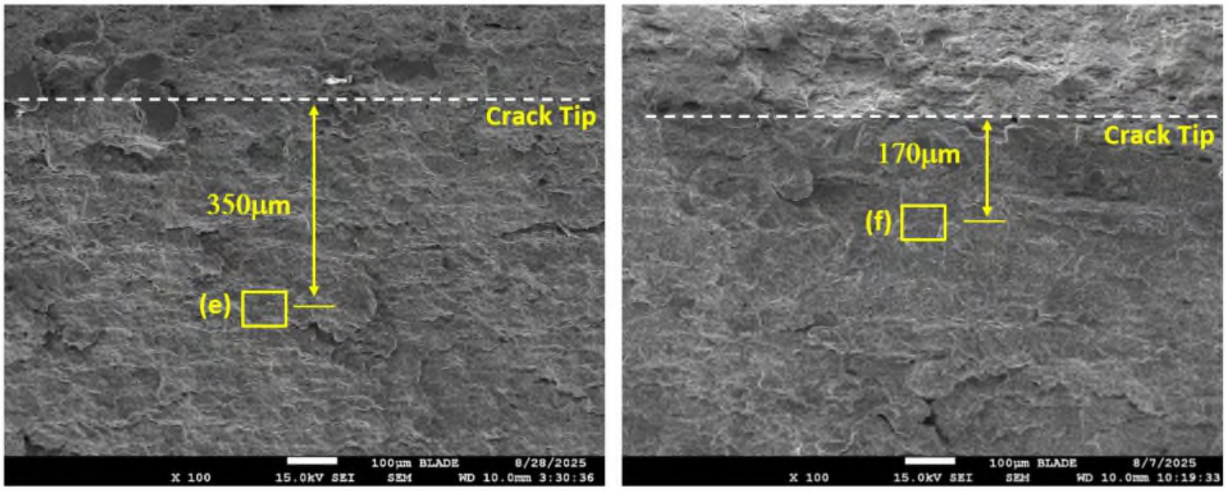

Figure 17: SEM fractograph map near crack tip

Fatigue stiations represent a small area fraction in the regions depicted in Figure 18 350 µm below the crack tip, and in Figure 19 170 µm below the crack tip. In this region of the HAZ, where the crack may be approaching or entering the outer CGHAZ, environmentally assisted cracking is the dominant crack advance mechanism. Supporting evidence of an environmental effect is the presence of crystallographic etch pits in each location. A high-magnification micrograph of the outer CGHAZ was not available for comparison with the initiation region.

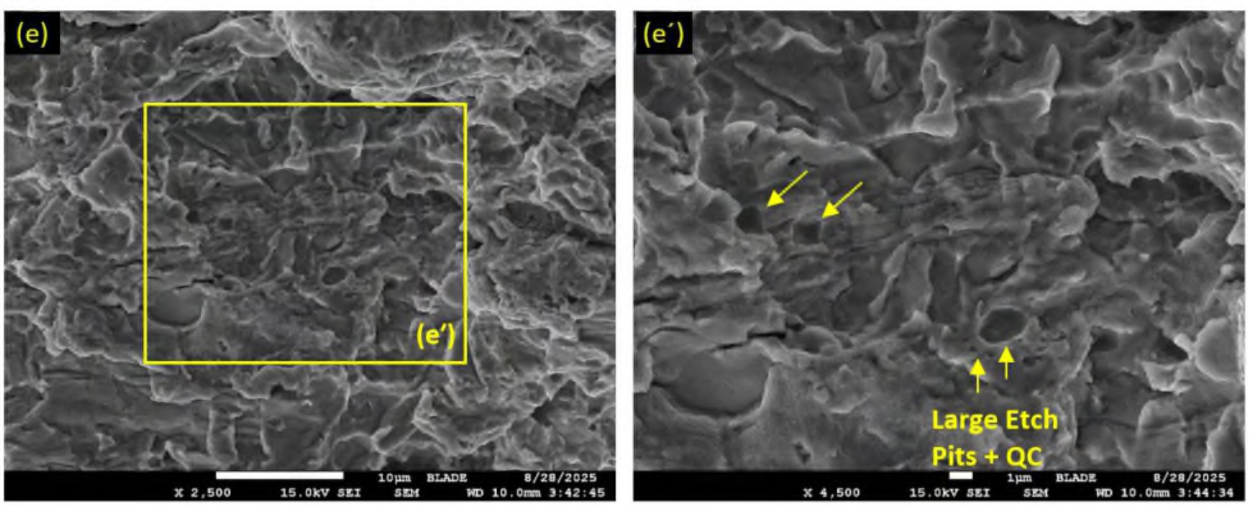

Figure 18: SEM fractography, 600 µm below crack tip

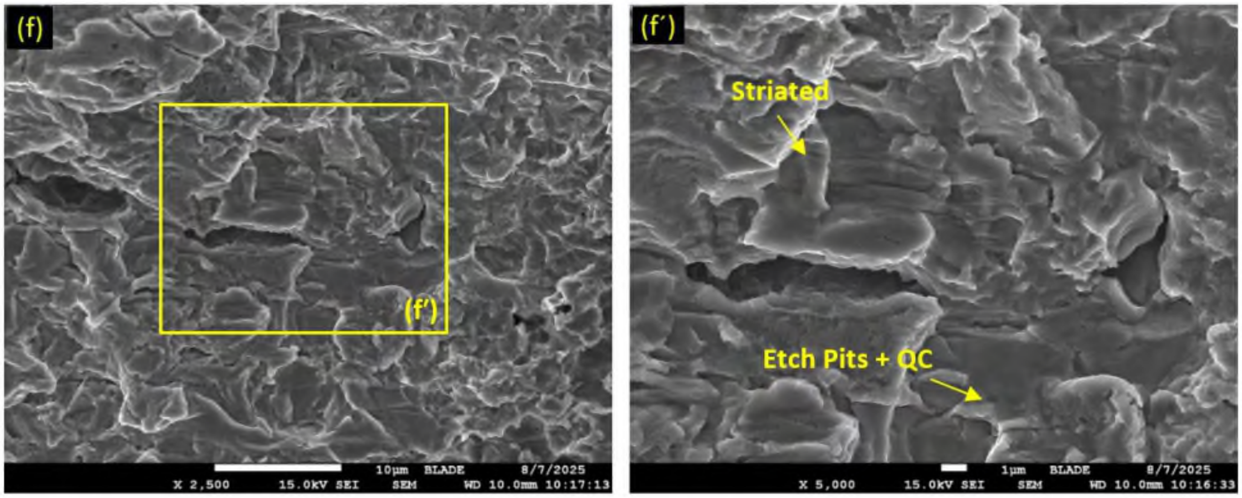

Figure 19: SEM fractography, 420 μm below crack tip

4.2.4 Striation Evaluation

A first iteration striation count was performed using three micrographs of progressive crack lengths, including the ID, midwall, and crack tip just before failure. The locations evaluated and results are shown in Figure 20. A steady increase in striation spacing is evident. It is worth noting that, as a secondary effect, in regions with increasing area fractions of phases that experience crystallographic fracture, isolated striation counts/spacing may misrepresent or underestimate the overall crack growth rate.

Ritchie et.al. [12] showed that high mean stress in steel under carefully controlled conditions can promote cleavage in microphases, where a combination of striated growth in some phases and isolated cleavage “bursts” in other phases works in concert to produce a faster apparent crack growth rate than measured at lower mean stress in a completely striated matrix. Comparative fractography in [12] shows fatigue striations in a striated crack growth, and in partially striated fracture exhibits similar spacing at different da/dN rates. Ritchie makes the statement that striated growth may be independent of Kmax (maximum stress intensity) at the crack tip.

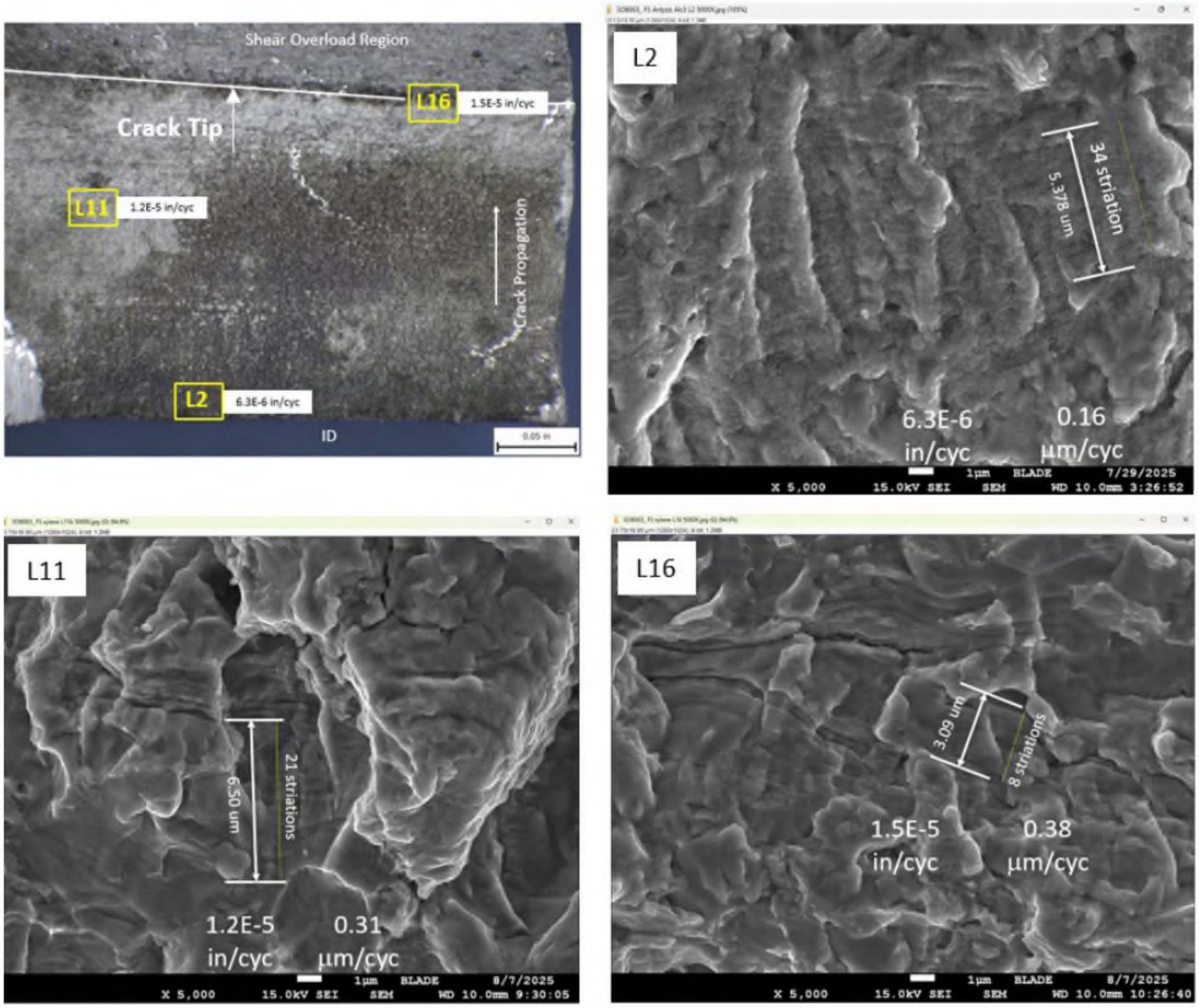

Figure 20: Striation counts

4.2.5 Conclusion on Cracking in the HAZ

In short, the morphology of the fatigue fracture surface varies from ID to OD. Closer to the ID, up to around 5 to 10% of the wall thickness has a striated fatigue fracture surface, which supports crack propagation in air. However, beyond 10% of the wall thickness, the fatigue fracture mode, still striated, exhibits more quasi-cleavage/cleavage, indicating hydrogen-enhanced fatigue crack growth.

Fatigue striations are found distributed throughout the subcritical crack face. Fatigue striations at the ID appear to be more closely spaced, indicating slower crack growth rates.

Microstructural phases preferentially exhibit fatigue striations. Etch pits are found covering the surface, suggesting cleavage was occurring preferentially in a given phase fraction. This phase fraction varied over the HAZ. The dissolution of large secondary particles suggests that given phases in the microstructure are susceptible to environmentally assisted or enhanced crack growth in a cyclic load scenario.

Zhao [10] showed fatigue crack growth rates in air at R=0.1 at ΔK levels in the Paris regime through the CGHAZ, FGHAZ, and ICHAZ, which do not vary. Therefore, an environmental effect is likely enhancing the crack growth rates, as the fracture surface exhibits both quasi-cleavage and cleavage features.

4.3 J-R Fracture Assessment

Anderson performed J-R testing using compact tension (CT) specimens at -5°C per ASTM E1820 [13]. The specimens were oriented in the C-L orientation [14].

In this section, examples of HAZ from pipes used in the pipeline, as well as unused pipes, are compared. An example of a CT sample with W = 0.992 in. and B = 0.322 in., with its orientation and notch placement with respect to the HAZ, is shown in Figure 21.

(b)(4)

Figure 21: Notch placement within HAZ, J-R CT specimens

Multiple base, Weld, and HAZ specimens were tested. The focus in this section is the HAZ.

Anderson conducted three sets of J-R tests, which are summarized below.

- HAZ specimens from the failed joint, shown in Figure 22. The Ju ranges from (b)(4) as shown in Figure 22.
- HAZ specimens from the failed joint, Bake out at 400°F for 30 minutes. The Ju ranges from (b)(4) (b)(4) as shown in Figure 23.
- HAZ specimens from an unused Berg joint. The Ju ranges from (b)(4) as shown in Figure 24.

(b)(4) [redacted]

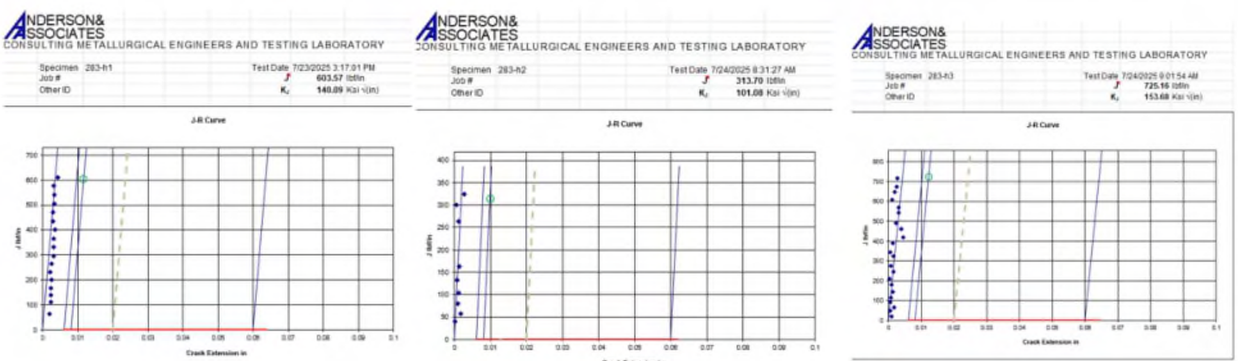

Figure 24: J-R test data at -5°C for unused Berg pipe HAZ

J-R tests with the crack located in the HAZ exhibited cleavage behavior, while some welds remained ductile. For this reason, further investigation of the HAZ was warranted.

The ASTM E1802 [13] J-R test records for HAZ sample JH1-324-32-9, taken from the failed joint, are shown in Figure 25. The HAZ specimen attained a J value of (b)(4) [redacted] A review of the fractographic evidence, as shown in Figure 22, exhibits (b)(4) [redacted] There was no ductile-brittle transition temperature (DBTT) test conducted for the HAZ; however, literature data indicate that it would typically be -30 °C. (b)(4) [redacted] To further analyze this, J-R testing was conducted for an unused sample of X70 pipe that South Bow had in inventory, as shown in Figure 24.

The results of that test with the unused sample 283-H1 X-70 HAZ are shown in Figure 26. The unused HAZ had a J value of around 610 lbf/in and failed in an unstable fashion as well. The fractographic evidence shows cleavage morphology.

This is significant because any impact of the operating environment was absent from the unused pipe. The HAZ was clearly brittle before being put into operation. The manufacturing process is responsible for the brittleness.

The behavior of the used and unused material must be further investigated in the context of the HAZ microstructure. After establishing DBTT, further analysis of the J-R at operating temperature is necessary to understand the behavior at ambient conditions. This activity is needed after completion of the RCFA.

(b)(4)

[redacted]

(b)(4)

[redacted]

4.4 Residual Stress Measurement

Residual stress measurements were taken near the external and internal weld roots using the hole drilling method per ASTM E837 to determine the stress state at the surface. The measurements were taken on a section of the failed joint upstream of the failure and on the joint downstream of the failure. Figure 27 shows the location of the residual stress measurements. Corner gauges were used to position the rosette as closely as possible to the weld root.

Figure 28 shows the results for the OD and ID of the failed joint section. The x-stress is longitudinal and the y-stress is hoop. The results show that the hoop stress at the OD and ID locations is in compression. The OD reaches a maximum compressive stress between 20 and 30 ksi, whereas the ID reaches approximately 70 ksi. Figure 29 shows the results for the downstream joint. These are consistent with the failed joint, except that the compressive stress range is generally lower.

The results are consistent with the FEA conducted in Section 5.4.2, which shows a residual compressive stress at the ID after the pipe experiences a hydrotest.

(b)(4)

[redacted]

Figure 28: Residual stress at the OD and ID of the failed joint

(b)(4)

[redacted]

4.5 Conclusions

- The fatigue propagation region exhibits at least two distinct areas. The region adjacent to the ID was typical of fatigue crack growth rate in air, interpreted by the fractographic evidence. The next region, beyond a 10% wall thickness, was characterized by more quasi-cleavage and cleavage with striations, indicating a hydrogen-enhanced fatigue region.
- The LECO test results exhibit higher hydrogen levels in the used HAZ/weld/base metal when compared to unused samples. This implies the introduction of an additional hydrogen into the metal during the transportation of crude oil.
- Cleavage and unstable J-R imply a compromised microstructure that may be more susceptible to environmental cracking. This needs to be investigated further.
- Compression residual stresses were noted on the ID and OD; perhaps due to the hydrostatic test.

5 Fatigue and Fracture Assessments

Anderson found that the cause of the MP 171 rupture near Fort Ransom was fatigue cracking that initiated at the toe of the seam weld on the ID. Blade reviewed the Anderson report and performed additional metallurgical analysis to confirm the Anderson conclusions. Blade's review of the Anderson findings and the additional laboratory work is discussed in Section 4. This section presents the fatigue and fracture analyses used to confirm the Anderson conclusions and Blade's proposed sequence of events.

Fatigue cracking is a sub-critical cracking mechanism that involves initiation, growth, and final fracture. Cyclic loading forms slip band intrusions and extrusions at the surface, which can act as localized stress concentrations, leading to the nucleation or initiation of fatigue cracks. Continued cyclic loading will eventually form microcracks that grow into macro fatigue cracks. Fatigue initiation is primarily dependent on the material, surface conditions, and localized stresses, impacted by the local stress concentration factor (SCF). SCF within a structure, at a discontinuity, such as a weld toe, is a significant factor in fatigue crack initiation, even when the overall stress of the structure is low.

Once initiated, crack growth is separated into two stages. Stage I is characterized by microcrack growth that occurs near the fatigue nucleation site and is primarily driven by shear. This then transitions to a macro crack, Stage II, when the crack grows perpendicular to and is driven by the maximum tensile stress range [15]. The initiation and growth of defects primarily determine the fatigue life of a structure. The final fracture is instantaneous and occurs when a critical crack size is achieved, causing the structure to fail.

Total fatigue life is the sum of the initiation life and propagation life. Depending on the magnitude of cyclic stress (or strain), initiation life or propagation life can dominate the total life. As Figure 30 shows, at low stress amplitudes, initiation life is the dominant contributor to total life, supporting the common assumption that total life is equal to initiation life. With increasing stress amplitude, propagation life becomes an essential contributor to total life. Fatigue initiation is not required if microcracks preexist in the material from manufacturing or loading that occurred before exposure to service conditions. In cases where microcracks exist, the fatigue life consists entirely of growth, followed by the final failure.

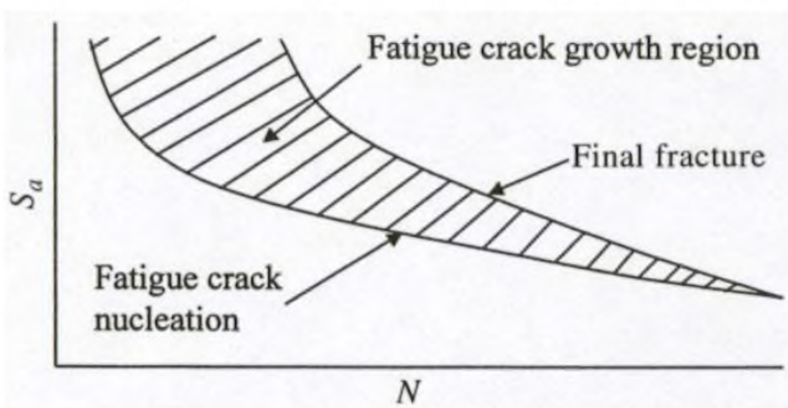

Figure 30: Effect of stress amplitude on the contributions of initiation and propagation life [15]

Blade performed a fatigue assessment to estimate the number of cycles required for crack initiation, growth, and final failure.

The approach here begins by confirming the critical flaw size for the final unstable failure, and is discussed in Section 5.1. Crack initiation is discussed in Section 5.4, and crack propagation in Section 5.2.

The results from this section shall address the following questions:

- What was the critical crack size at the time of the failure?
  - Do the assumed crack size and material properties match the actual events of the failure?
- Could a crack initiate and grow to failure during the 15 years the pipe was in service, given the known pressure cycles applied to the pipeline?
  - If not, what initial crack size is required to meet the timeframe of the failure, and how did the preexisting crack develop before service?
  - What fatigue crack growth parameters (Paris Law coefficients) were likely in the crude oil environment, and could they grow a crack to failure during the service life?
- How did the weld geometry and material properties contribute to the fatigue initiation and growth?

5.1 Critical Crack Size Evaluation

The critical crack size is the point at which a crack reaches a length and depth sufficient to rupture the pipe at a given pressure. The evaluation utilizes material properties, pressure at the time of failure, and the final crack size to demonstrate that the rupture should have occurred from a fracture mechanics perspective. The analysis does two things:

1. Confirms the final crack size determined during the metallurgical analysis
2. Confirms the material properties (tensile and fracture) measured at the HAZ

Blade used Crack Analyzer 2.5, an internal software package that is based on API 579/ASME FFS-1-(2021) [16] , to perform Level 2 analyses. API 579 utilizes the Failure Assessment Diagram (FAD) approach to assess the integrity of a pipeline, particularly for crack-like flaws.

API 579 permits three levels of assessment for crack-like flaws. As the level of assessment increases, conservatism is reduced, analysis complexity increases, and the amount of required data, such as loading, flaw size, and material properties, increases. Level 1 and 2 assessments are used to evaluate crack and crack-type flaws in structural components for fitness-for-service purposes. In contrast, FAD Level 3, which involves a material-specific FAD and ductile tearing instability analysis, is used to predict burst pressure and leak/rupture for high-toughness ductile materials. A level 3 assessment was not performed because the J-R curves were not ideal for running the analysis.

5.1.1 API 579 Level 2 Assessment

Blade first performed a Level 2 assessment, which required the pipe dimensions, final crack dimensions, material properties, assessment pressure, and material toughness. The failed pipe had a 30 in. nominal OD and 0.386 in. nominal wall thickness. The final crack dimensions were estimated from the Anderson report. Figure 31 shows the Anderson measured fatigue crack profile. The maximum depth wa[redacted] in. [redacted] NWT) and occurred 15.5 in. upstream from GW610. The total reported length of the fatigue crack was [redacted] in. The API 579 equations assume a semi-elliptical shape, which is inconsistent when considering the full-length crack profile and the apparent three-lobed nature of the profile. The estimated crack length, based on a semi-elliptical crack shape that covers the deepest and central lobe, is 7.5 in. Figure 32 shows the assumed crack shape, superimposed onto the fracture surface. The scaled length of the assumed shape was 7.75 in.

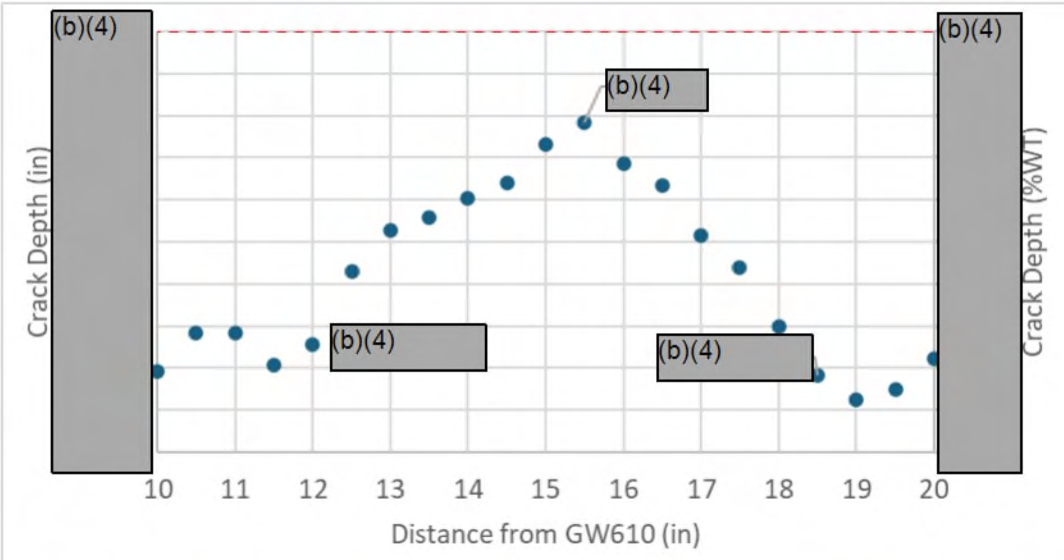

Figure 31: Fatigue crack profile extracted from the Anderson report [17]

Figure 32: Macro image of fatigue crack [17]

The pressure at the time of failure was determined using SCADA data provided by South Bow. Figure 33 shows the pressure data closest to the pump station. The rupture occurred at 6:42 AM MST on April 8, 2025. The plot shows that the pressure at the time of rupture was (b)(4) kPa (b)(4) psi). The rupture occurred at the end of a pressure cycle that began at a peak pressure of (b)(4) kPa (b)(4) psi) at 4:40 AM MST and reached a minimum of (b)(4) kPa (b)(psi) at 5:39 AM MST. The MOP of the Keystone pipeline is 1,440 psig.

(b)(4) [redacted]

The Level 2 FAD incorporates tensile and fracture toughness properties in the analysis. Table 2 shows the tensile test results extracted from the Anderson report. The yield and tensile strength for the failed joint are (b)(4 [redacted] ksi and (b)([redacted] ksi, respectively. The tensile properties are consistent with the upstream and downstream joints, which had yield strengths ranging from (b)(4 [redacted] ksi to (b)(4 [redacted] ksi and tensile strengths from (b)(4) [redacted] ksi to (b)(4) [redacted] ksi. Table 3 show the tensile properties from the Edinburg rupture. The yield strengths are slightly higher than those of the Fort Ransom joints, but consistent with those of grade X70 pipe. The tensile strength values were consistent with those of the Fort Ransom joints and, more generally, with those of grade X70 pipe.

Table 2: Fort Ransom failure tensile testing results

Joint	Specimen	Material	Location Relative to Seam Weld	0.5% EUL Yield Strength (ksi)	Tensile Strength (ksi)	Yield to Tensile Ratio
Upstream	42-US2-11	Weld	0	(b)(4) [redacted]	[redacted]	-
Upstream	222-US2-11	Base Metal	180	[redacted]	[redacted]	0.76
Upstream	222-US2-5	Base Metal	180	[redacted]	[redacted]	0.79
Upstream	222-US2-7	Base Metal	180	[redacted]	[redacted]	0.80
Failure	324-33-9	Weld	0	[redacted]	[redacted]	-
Failure	144-33-9	Base Metal	180	[redacted]	[redacted]	0.81
Downstream	310-47-3	Weld	0	[redacted]	[redacted]	-
Downstream	130-48-2	Base Metal	180	[redacted]	[redacted]	0.80

Table 3: Edinburg tensile testing results

Specimen	Material	Location Relative to Seam Weld	0.5% EUL Yield Strength (ksi)	Tensile Strength (ksi)	Yield to Tensile Ratio
590-B1	Base Metal	180	(b)(4) [redacted]		0.89
590-B2	Base Metal	180			0.87
590-B3	Base Metal	180			0.88
590-W1	Weld	0			0.82
590-W2	Weld	0			0.82
590-W3	Weld	0			0.81

Blade measured the HAZ and weld tensile properties using a tabletop plastometer. The plastometer technology is a tabletop unit that estimates yield properties from a local indentation in the target material. Load and displacement are measured as the indenter is pressed into the target material. Load and unload cycles are performed until the desired depth is achieved. A profilometer is then used to measure the indent profile. Reverse finite element analysis is then used to estimate the stress-strain curve of the material, which provides the yield and tensile strength measurements. The advantage of the plastometer approach is that the measurement is localized to the material under and adjacent to the indenter.

Figure 34 shows the indentation locations on a weld extracted from the failed joint. Table 4 shows the estimated yield and tensile strengths. The HAZ and weld regions are consistent with the base metal values presented in Table 2. Note that the HAZ region is slightly lower than the base metal, but not enough to consider differences in the material behavior.

Vicker's microhardness readings were also taken across the weld on the left and right sides near the ID. Figure 34 shows the left and right indent regions. The values show that the hardness does not vary significantly between the base metal, HAZ, and weld regions. The minimum and maximum hardness values are 185.1 $HV_{0.5}$ and 275.3 $HV_{0.5}$, respectively. These values correspond to 90.1 HRB for the minimum value and 26.5 HRC for the maximum. On average, the HAZ region is slightly lower (212.1 $HV_{0.5}$) than the weld region (236.0 $HV_{0.5}$), which is consistent with the plastometer results.

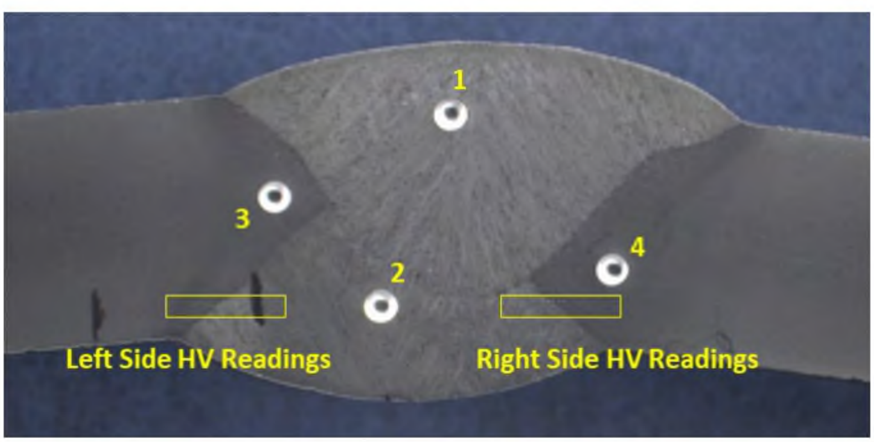

Figure 34: Tabletop plastometer indentation locations

Table 4: Estimated yield and tensile properties (tabletop plastometer)

Indentation	Location	Yield Strength (ksi)	Tensile Strength (ksi)	Yield to Tensile Ratio
1	Weld Cap	78.5	93.8	0.84
2	Weld Root	74.8	91.8	0.81
3	HAZ Left	69.8	85.9	0.81
4	HAZ Right	68.2	88.6	0.77

Table 5: Weld microhardness readings from the failed joint

Material	Indent	Left Side		Right Side	
		$HV_{0.5}$	HRB/HRC	$HV_{0.5}$	HRB/HRC
Weld	1	212.9	95.0	254.4	23.1
	2	208.1	94.6	269.8	25.6
	3	229.7	98.3	217.6	96.3
	4	260.7	24.0	232.3	98.7
	5	247.1	21.8	224.7	97.5
	6	249.4	22.2	225.3	98.0
Transition to HAZ	7	226.0	97.7	224.0	97.3
	8	275.3	26.5	202.3	93.5
HAZ Transition to Base Metal	9	234.1	99.0	214.3	95.7
	10	225.0	97.5	212.1	95.3
	11	230.9	98.5	202.8	93.6
	12	236.6	99.4	217.2	96.2
	13	218.0	96.3	211.5	95.3
	14	189.7	90.9	193.3	91.7
	15	185.6	90.1	191.5	91.3
	16	185.1	90.1	197.6	92.5
	17	198.3	92.7	215.1	95.8
	18	195.8	92.2	207.4	94.5

Fracture toughness is the resistance of a material to fracture and is measured in terms of the crack tip conditions. The parameters used to define the crack tip conditions are stress intensity factor (K), crack tip opening displacement (CTOD), and the J-integral (J). K is a parameter used to define the crack tip conditions of a linear elastic material. In contrast, the CTOD and J parameters are used to define the crack tip conditions in an elastic-plastic material.

Table 6 shows the fracture toughness results reported by Anderson. The HAZ values (JH1, JH2, and JH3) were chosen for use in the Level 2 analyses. Note that the values are a Ju qualification. The fracture toughness testing at Anderson is discussed in more detail in Section 4.3.

Table 6: Fort Ransom fracture testing results for the failed joint

Specimen ID	J (lbs/in)	J (N/mm)	Qualification	K_J (ksi√in)	K_J (MPa√m)
JH1-324-32-9	1,175	205.8	J_u	196	215.4
JH2-324-32-7	1,471	257.6	J_u	219	240.6
JH3-324-32-5	647	113.3	J_u	145	159.3
JW1-324-33-1	784	137.3	J_{IC}	160	175.8
JW2-324-32-11	1,036	181.4	J_{IC}	184	202.2
JW3-324-32-10	573	100.3	J_{IC}	137	150.5

Figure 35 shows the results from the API 579 Level 2 assessment. A sensitivity analysis was performed on the crack length and fracture toughness. Table 7 shows the API 579 Level 2 fixed inputs, which were well understood (with minimal variability) and remained constant during the sensitivity analysis. The results in Figure 35 show that the initial crack length can vary between [redacted] in. and [redacted] in. based on the variability in fracture toughness values for the HAZ region of the weld. The results suggest that the final crack length is between [redacted] and [redacted] in. However, Blade measured a final crack length of [redacted] in., which means a less conservative approach is required. An API 579 Level 2 material-specific analysis was conducted to refine the assumptions made regarding the critical crack size and material properties.

[redacted]

Figure 35: [redacted]

Table 7: Fixed inputs for API 579 Level 2 assessment

Nominal Outside Diameter (in)	30
Nominal Wall Thickness (in)	0.386
Failure Pressure (psi)	1,252
Maximum Operating Pressure (psi)	1,440
Failure Crack Depth (in)	0.302
Failure Crack Depth (%WT)	78.2
Yield Strength (ksi)	68.2
Ultimate Tensile Strength (ksi)	88.6

5.1.2 API 579 Level 2 Material Specific Assessment

The Crack Analyzer 2.5 has an option for a Level 2 material-specific analysis, which accounts for improved estimates on the tensile properties of the material. A material-specific analysis requires the Ramberg-Osgood (RO) parameters to generate a material-specific FAD curve. Blade has a database of true stress-strain data for various pipe grades, generated from true stress-strain testing conducted at Blade Energy Laboratories. The true stress-strain data were generated using Blade's custom vision system to track instantaneous specimen dimensions during a typical tensile test. Blade selected representative data for the base metal and weld material of grade X70 pipe.

Figure 36 shows the engineering stress-strain curves for the selected base metal and weld materials. The calculated yield and tensile strengths are displayed on the plot. The yield properties for the base metal and weld are consistent with the reported values in the Anderson report, as well as the estimated values from the tabletop plastometer.

Figure 37 shows the corresponding true stress-strain data for the same materials. Note that the data plotted in Figure 37 is measured true stress-strain data and is not an estimated curve converted from the engineering stress-strain data. The calculated RO parameters from the true stress-strain data are displayed on the plot and were calculated based on the following equation:

$$\frac{\epsilon_{ref}}{\epsilon_{ys}} = \frac{\sigma_{ref}}{\sigma_{ys}} + \alpha\left(\frac{\sigma_{ref}}{\sigma_{ys}}\right)^n \qquad (1)$$

The strain hardening coefficient, n, and alpha values were used as inputs to the material-specific Level 2 assessment. Figure 38 shows the results from the material-specific Level 2 analysis. The three curves represent the three J-integral values from the Anderson HAZ testing. The x-axis is the crack length, and the y-axis is the calculated limiting pressure. A limiting pressure equal to the failure pressure [redacted] psi) occurs at the critical crack size. The plot shows that the critical crack length, assuming a failure depth of 0.302 in., is 5.45 in., 8.63 in., and 10.33 in., for the different toughness values.

The results show that the material-specific FAD removed conservatism from the calculation, thus increasing the critical crack lengths. The crack length estimated from the Anderson report is [redacted] in.; the length was chosen based on the elliptical profile of the crack. This estimate of length was used with the fracture toughness of [redacted] si√in. The estimated failure or limiting pressure was [redacted] psi; less than [redacted] difference from the actual pressure at failure of [redacted]si. This validates the metallurgical analysis of the subcritical crack region and the estimation of [redacted] in.

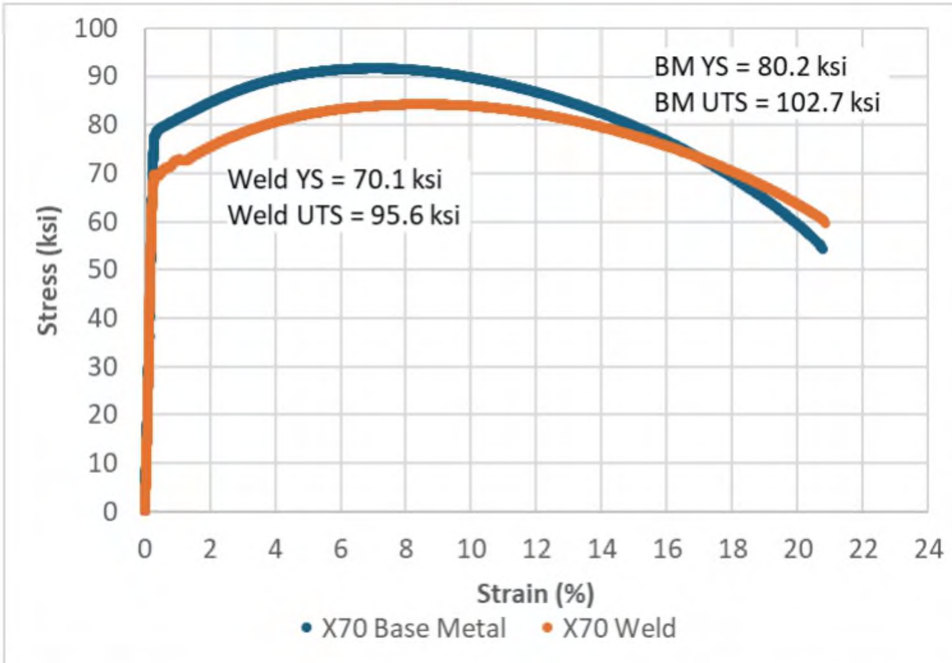

Figure 36: Engineering stress-strain curves for grade X70 pipeline steel

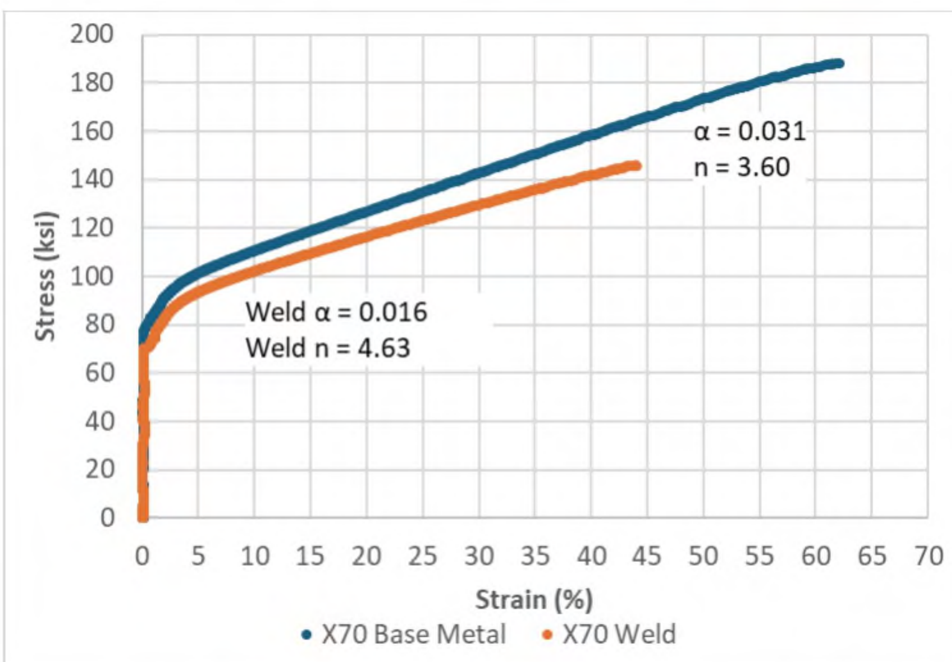

Figure 37: True stress-strain curves for grade X70 pipeline steel

(b)(4)

[redacted]

Figure 38: API 579 Level 2 assessment results at different toughness values

5.2 Crack Growth Analysis

Crack growth occurs after initiation and continues until the critical crack size, determined in Section 5.1, is reached. The objective of this analysis is to estimate the time required to grow a crack from an assumed initial size to the critical crack size. The results from the fatigue crack growth analysis will indicate whether a crack can initiate and grow to failure during the pipe's lifetime. The pipe was in operation for approximately 15 years, from the installation in 2010 to the failure on April 8, 2025. The results from the analysis took into account the fact that, in high-cycle fatigue (characterized by a small stress range), most of the fatigue life is spent in the initiation phase. For initiation and growth to occur during operation, the growth phase must occur within 3 to 5 years.

The fatigue crack growth rate (FCGR) is a measure of the crack extension per cycle in a material. The FCGR is used to determine remaining life in structures and is a function of the applied stress intensity range. Higher values of ΔK result in higher crack growth rates and are typically plotted against ΔK on a log-log plot. The result is a sigmoidal-shaped curve with three regions:

Region I – Near Threshold

Region II – Stable Growth

Region III – Rapid Growth

Figure 18 illustrates the typical fatigue crack growth curve, with the three regions clearly identified. Region I is characterized by the K threshold range, K_{th}, below which cracks either propagate at a slow rate or do not propagate at all. Above the K_{th} value, the crack growth rate increases rapidly, leading to Region II. Region II is modeled by a power function, with the most common being the Paris Law equation (Equation 2). Region III approaches a maximum stress intensity range, K_{max}, that is equal to the critical stress intensity factor K_c.

$$\frac{da}{dN} = C(\Delta K)^m \tag{2}$$

The Paris Law equation is defined by two parameters, C and m. The API 579 recommends values of 3.60E-10 in/cycle/(ksi√in)^m [6.89E-9 mm/cycle/(MPa√m)^m] for C and 3.0 for m for pipeline steels in a non-aggressive environment (air). The API 579 also recommends values of 3.80E-9 in/cycle/(ksi√in)^n [7.27E-8 mm/cycle/(MPa√m)^n] for C and 3.0 for m for pipeline steels in a marine environment. Additional environments were also considered based on results from the fractographic examination of the fracture surfaces.

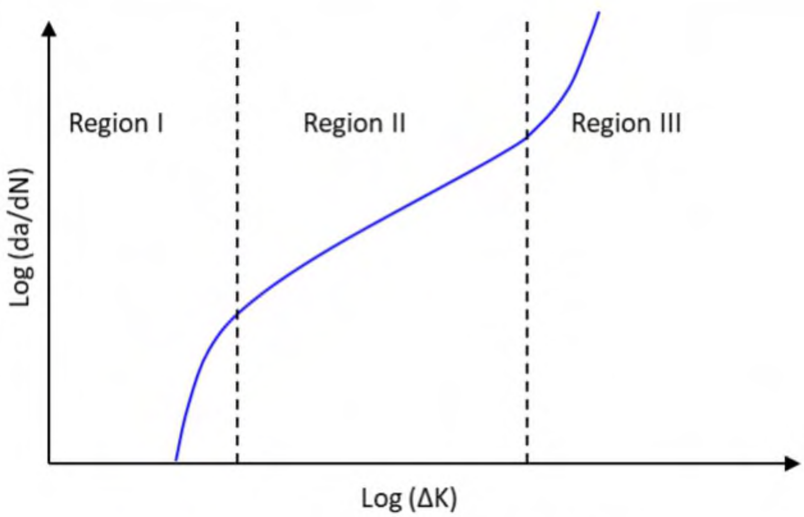

Figure 39: Typical fatigue crack growth curve

Blade confirmed the Anderson report by identifying fatigue striations from the ID to the OD. However, a change in surface morphology was observed beginning at a depth of 5%-10% from the ID surface. Up to approximately 10% deep, the striations and surface morphology were consistent with fatigue in air. Beyond the 10% depth, the striations were intermittent, and cleavage was identified in most areas. The observation suggests a change from air fatigue to environmentally assisted fatigue. Blade interpreted the change as the difference between transportation fatigue and pressure cycle fatigue during the pipeline operation.

To investigate the effects of the production environment, discussed in Section 7, FCGR in more aggressive environments was also considered. Table 8 shows the various Paris Law coefficients considered, along with their corresponding environments. Figure 40 is a plot of the data presented in Table 8. There are multiple possibilities; one is that the crude oil is benign and the HAZ microstructure is optimal, with FCGR behavior similar to that in air. However, the fractographic evidence points towards a hydrogen-enhanced fatigue. The most relevant data set from literature would be electrochemically generated hydrogen, which could be under free corrosion or cathodic protection. Corrosion fatigue under free corrosion or under CP is due to hydrogen-enhanced fatigue crack propagation. In the absence of testing, Blade decided to use the upper-bound curve from API 579 and BS 7910 as being representative for this analysis.

Table 8: Paris Law coefficients

	Source	Alloy	Condition	m	C (mm/cyc/(MPa√m)^n
1	API 579 EQN 9F.94 [16]	Ferritic Steels	Air	3.00	1.65E-09
2	API 579 EQN 9F.98 [16]	Ferritic Steels	Marine	3.00	7.27E-08
3	API 579 EQN 9F.104 [16]	Ferrite-Pearlite Steels	Air	3.00	6.89E-09
4	Gangloff Article [18]	X-70 NaCl	3.5% NaCl, -1000mV SCE	0.496	1.72E-04
5	Gangloff Article [18]	X-65 NaCl (1)	3.5% NaCl, -1000mV SCE	0.044	5.08E-04
6	Gangloff Article [18]	X-65 NaCl (2)	3.5% NaCl, -1000mV SCE	0.077	7.07E-04
7	Gangloff Article [18]	BS-4360	3.5% NaCl, -1000mV SCE	0.044	4.04E-04
8	BS 7910 (Section 8.2.3.5)	Welded Steels Simplified	Free corrosion	3.00	7.27E-08
9	BS 7910 (Table 11)	Welded Steels Stage 1 of 2	Free corrosion	3.42	1.15E-08
10	BS 7910 (Table 11)	Welded Steels Stage 2 of 2	Free Corrosion	1.30	1.72E-05

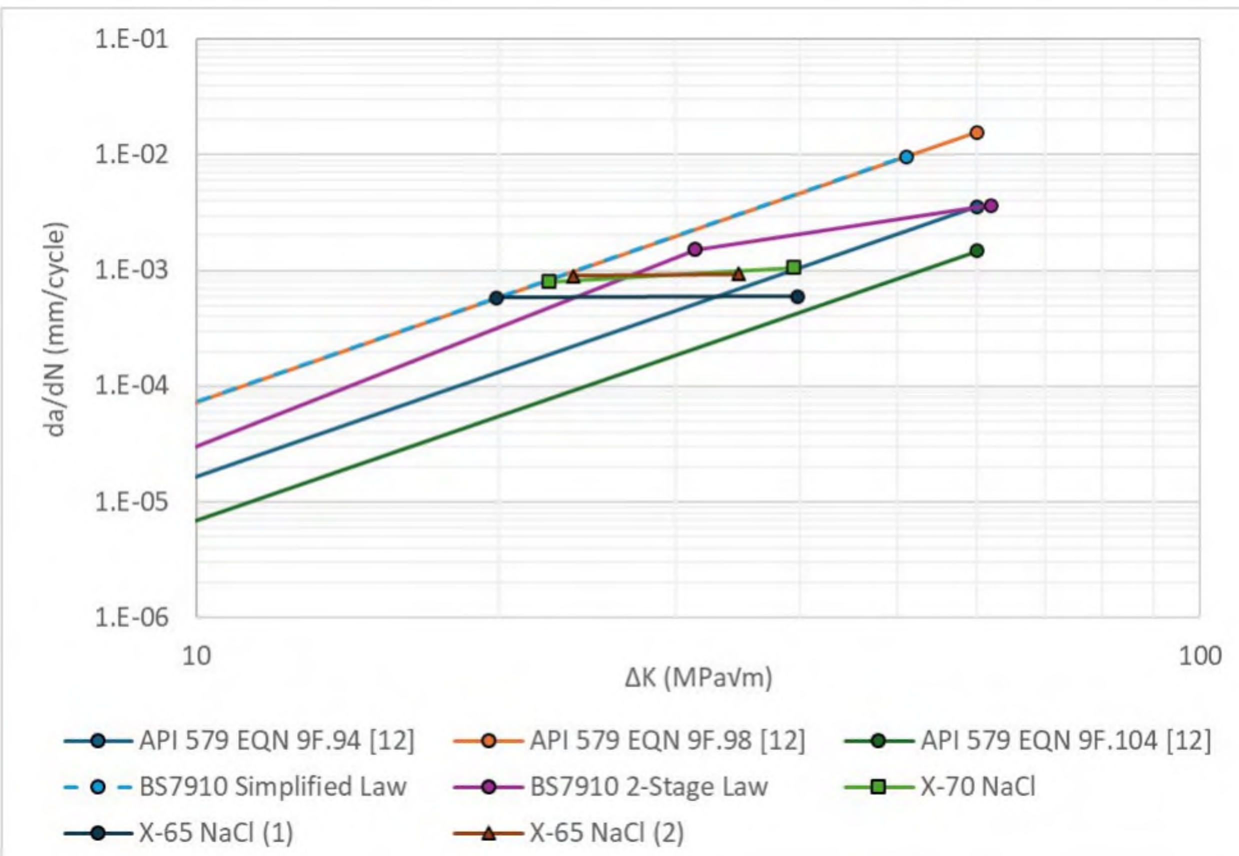

Figure 40: Fatigue crack growth rates in various environments

The primary loading during crude oil transportation is pressure; other loads such as thermal would impact a circumferential cracking, and not applicable to axial cracking.

Loading cycles must be characterized to perform an API 579 Level 2 fatigue assessment. South Bow provided SCADA data for each year the pipeline was in service (2010 to 2025). Blade performed a rainflow analysis for each year using Crack Analyzer 2.5. Rainflow analysis is a method for counting the number of pressure cycles in a given data set and categorizing them into distinct pressure cycle bins. Miner's rule is then used to generate an equivalent pressure cycle and cycles per year for a constant amplitude pressure range assumed for the analysis that approximately represents the damage applied to the pipe from the actual pressure cycles. The results are summarized in Table 9 and are graphically shown in Figure 41.

The equivalent cycles are not set to the MOP value of 1,440 psi because the Crack Analyzer 2.5 software uses the maximum cycle measured from the pressure data instead. Each year was processed independently, which explains the year-to-year difference in the equivalent cycles in Table 9.

The graph shows a decreasing trend in cycles per year beginning in 2013. An average equivalent pressure and cycles per year were used for the fatigue analysis. 2010, 2011, and 2025 were not included in the averaging process. 2010 and 2011 were significantly different from the other years, and 2025 was only a partial year due to the failure. The averaged values used for the analysis are 1,348 psi and 38 cycles per year.

Table 9: Rainflow analysis of SCADA data from 2010 to 2025

Year	Equivalent Pressure (psi)[1]	Equivalent Pressure (kPa)[1]	Cycles/Year
2010	(b)(4) [redacted]		
2011			
2012			
2013			
2014			
2015			
2016			
2017			
2018			
2019			
2020			
2021			
2022			
2023			
2024			
2025			
Note 1: Equivalent pressure calculated by the Crack Analyzer 2.5 software and is the maximum pressure range in the data			

[redacted]

Figure 41: Equivalent pressure and cycles per year

Figure 42 shows the years to failure versus the initial crack depth for three different environments: API air, API marine, and BS 7910 free corrosion. The chosen inputs for the analysis are included at the top right of the figure. The study shows that a crack must pre-exist within the pipe during operation for it to reach a critical crack size in 15 years. The highest FCGR is the API 579 EQN 9F.98 environment (marine), and a 12% deep and 7.75 in. long crack is required for it to grow to failure by the 2025 rupture date. As discussed previously, it represents a hydrogen-enhanced fatigue that is consistent with fractographic data.

Crack Analyzer 2.5 was used to estimate the crack depth for each year of service from 2010 to 2025 based on the API 579 equation 9F.98. The API 579 equation 9F.98 was chosen because the fractographic evidence indicated that the transition between air and environment fatigue occurred approximately at that depth. A Level 2 assessment was used to grow the crack each year, using the equivalent pressure and number of cycles from Table 9. Figure 43 shows an estimate of crack growth versus time. The plot indicates that approximately half of the growth occurred from 2022 to 2025.

The plot also shows that the failure occurs when the crack is [redacted] in. long and [redacted] deep. The critical depth is shallower than the measured [redacted] because the Crack Analyzer 2.5 software does not perform a material-specific Level 2 assessment when conducting fatigue calculations, leading to a more conservative (shallower) critical crack size. Despite the discrepancy, the plot is a good representation of the estimated crack size over time.

The crack versus time plot indicates that the crack depth at the time of the [redacted] ILI tool run (2020) was [redacted]. The actual depth in 2020 is [redacted] when considering the conservatism associated with the API 579 Level 2 assessment.

(b)(4)

[redacted]

Figure 42: Years to failure based on API 579 level 2 fatigue assessment

(b)(4)

[redacted]

The crack growth analysis indicates that a preexisting crack is necessary for the crack to grow to failure, suggesting that loading before installation is required to initiate a crack. Transportation fatigue is the only loading source, prior to installation, capable of initiating and growing a crack. Transportation fatigue refers to the application of repeated stress cycles resulting from the handling and transportation of pipes.

Blade did not perform a transportation fatigue analysis to determine if a crack could initiate and grow during the transportation from the mill to the construction site. Instead, Blade relied on the work conducted by RSI for the Edinburg failure. RSI performed an FEA for the failed weld and a random vibration analysis to assess the potential for transportation fatigue. Figure 44 is a schematic from the RSI report showing the pipe stacking and deflected shape for the transportation analysis. RSI concluded that:

(b)(4) [redacted]

The MP 171 failed pipe had a similar weld geometry to the failed Edinburg pipe, suggesting that the MP 171 failed pipe was susceptible to transportation fatigue if positioned at a high stress area (near a contact point). It was not possible to determine the position of the failed joint in the pipe stack or the orientation of the seam relative to the contact points. The analysis only shows that initiation due to transportation fatigue is possible.

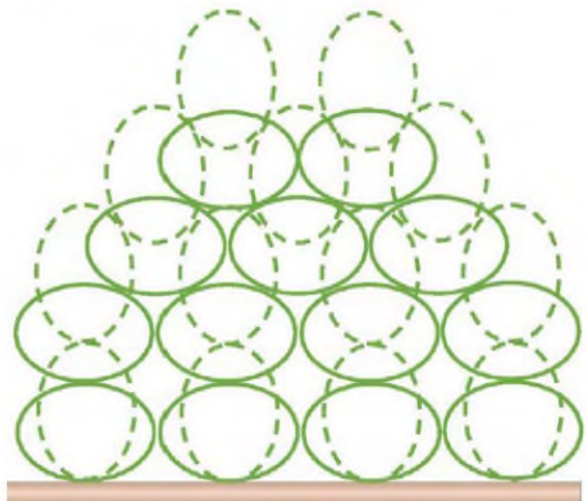

Figure 44: Vertical vibration of a pipe stack [19]

5.3 Hydrostatic Test Analysis

The crack growth analysis determined that a preexisting crack was necessary for the crack to grow to failure in 15 years. The results suggest that the preexisting crack was initiated and grew to the initial size through transportation fatigue. The implication is that the crack existed at the time of the hydrotest and should show a tearing band on the fracture surface. Tearing due to a hydrostatic test was not observed by Anderson on the fracture surface. However, tearing bands can be challenging to identify or nonexistent if the crack is shallow.

Blade conducted an API 579 Level 2 FAD assessment to determine if ductile tearing was likely for a given initial crack size. Figure 45 shows a sentence plot with the two initial crack sizes determined in Section 5.2. The plot shows that a 7.75 in. long crack with an initial depth of 12% is within the FAD curve and will not experience significant tearing, meaning the 12% crack could have existed during the hydrotest. The

35% depth is unlikely because it falls outside the FAD curve, indicating that tearing would occur; however, a tearing band was not observed during the metallurgical analysis.

(b)(4)

[redacted]

5.4 Crack Initiation Analysis

Crack initiation life is usually calculated using strain-life models (rather than the stress-life models used in the S-N approach). These models are mechanistic, based on material response to cyclic loading, and use experimentally determined material properties. The properties can be obtained directly through standardized experiments for the materials being used if samples are available, making it more directly applicable to the structure in question. Although their application in low-cycle fatigue problems is better known, strain-life methods are commonly used in general fatigue analysis problems, particularly when material properties specific to the material (or weldment) being used are available. Strain-life methods are most widely used for analyzing in-service structures, particularly to determine their remaining life. Since the approach is based on the micromechanics of fatigue and utilizes experimental data on material properties, it provides a more realistic estimate of fatigue life that suits the purpose of remaining life analysis for in-service structures.

In theory, the S-N method, which is based on testing to fatigue failure, would be expected to predict the total life of the structure, and is more of a design tool. Here we are trying to estimate initiation life realistically, so the initiation life method (ILM)-FCGR total life would be more appropriate. ILM-FCGR approaches are mechanistic, based on the material's response to cyclic loading, utilizing experimentally determined material and fatigue properties, and explicitly considering environmental conditions. Since the property data are obtained for the in-service materials, they are more representative of the fatigue response of the structure. A further limitation of the S-N approach is that it cannot be used to examine the remaining life of a structure with an existing defect. The mechanistic basis of the ILM-FCGR approach, its reliance on experimental data specific to the in-service material and service conditions, and its ability to characterize initiation life separately from crack propagation life, make it more suitable for analysis of the remaining life of structures in service. Both approaches are subject to uncertainties, which are covered through conservative choices of parameters and application of factors of safety, though, for reasons discussed above, it is common to use much lower factors of safety in ILM-FCGR than in the S-N approach.

Blade used the modified Smith-Watson-Topper (SWT) equation, given by Equation 3, to estimate initiation life. The SWT equation has been shown to correlate mean stress data better for a wider range of materials, and is therefore accepted as most promising for general use across a wide range of stress and strain amplitudes [20].

$$\sigma_{\max}\varepsilon_a E = \left(\sigma_f^{'}\right)^2 \left(2N_f\right)^{2b} + \sigma_f^{'}\varepsilon_f^{'} E\left(2N_f\right)^{b+c} \tag{3}$$

where,

ε_a is the (true) strain amplitude corresponding to the cyclic stress range,

σ_{max} is the maximum stress in a given cycle (or bin in a stress histogram),

E is the modulus of elasticity,

N_f is the number of cycles to failure (is the number of strain reversals to failure),

$\sigma_f^{'}$ is the fatigue strength coefficient,

$\varepsilon_f^{'}$ is the fatigue ductility coefficient,

b is the fatigue strength exponent, and

c is the fatigue ductility exponent.

The SWT equation argues that life scales inversely with $\sigma\varepsilon_a$. This product may be interpreted as the maximum strain energy density increment contributing to damage. Thus, the maximum stress is an important driver of life. The greater the magnitude of the maximum stress, the lower the predicted life. Mean stresses (including static loads and residual stresses) are therefore significant in life prediction.

The strain components are resolved into elastic and plastic components. The strain component curves are approximated on the log-log plot by straight lines represented by Equations 4 and 5. Figure 46 shows a schematic of the strain-life curve. The black curve represents the total strain amplitude, the red line represents the plastic strain component (Equation 5), and the blue line represents the elastic strain component (Equation 4). The curve in Figure 46 is known as the Coffin-Manson-Basquin curve, and the associated parameters are typically referred to as the Coffin-Manson parameters.

$$\frac{\Delta\sigma}{2} = \sigma_a = \sigma_f'\left(2N_f\right)^b \tag{4}$$

$$\frac{\Delta\epsilon_p}{2} = \epsilon_f'\left(2N_f\right)^c \tag{5}$$

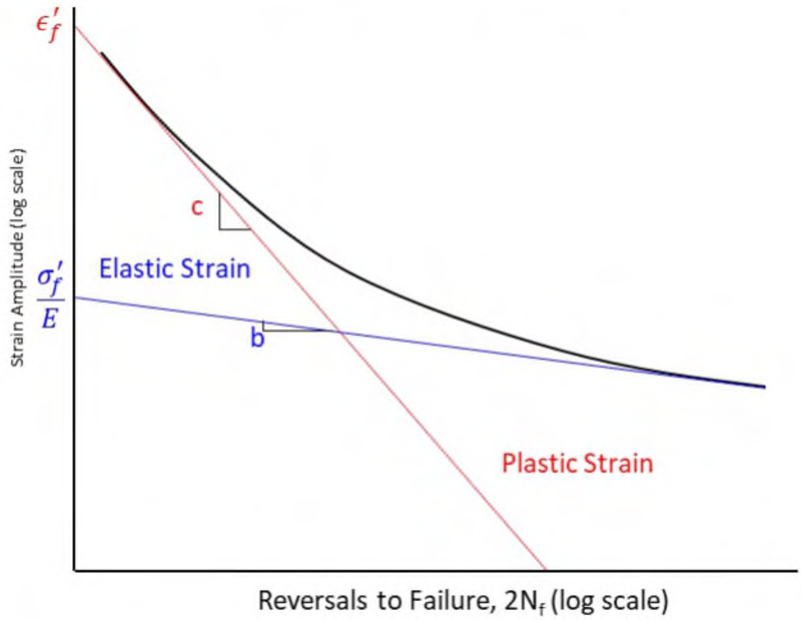

Figure 46: Strain-life curve

The SWT approach requires the strain amplitude and maximum stress during cyclic loading, as well as, the Coffin-Manson parameters $\sigma_f^{'}$, $\varepsilon_f^{'}$, a, and b. The strain amplitude is determined with FEA, which captures material properties and weld geometry to give an accurate estimate of the strain amplitude at the weld root radius. The Coffin-Manson parameters are ideally measured with laboratory testing. However, the testing is challenging and requires several specimens to generate the strain-life curve. The testing did not fit in the time frame of the RCA; therefore, estimated parameters were used from the literature.

5.4.1 Ductile Failure Damage Indicator

A technique for estimating crack initiation from large plastic deformation is the ductile failure damage indicator (DFDI). DFDI is a ductile plastic strain damage model derived from the concept that ductile failure results from the initiation, growth, and coalescence of voids on a microscale, as well as the formation of cracks following high plastic strains. The DFDI approach is applicable to the weld root radius because of the large local plastic deformation that could result in incipient cracking. Hancock and Mackenzie in the mid-70's followed Rice et al.'s work, and proposed a reference strain, ϵ_f , i.e., a strain limit for ductile failure, which is shown in Equation 6 and is expressed by stress tri-axiality, $\frac{\sigma_m}{\sigma_{eq}}$, and the material's critical strain, ϵ_0.

$$\epsilon_f = 1.65\epsilon_0 \, exp\left(-\frac{3}{2}\frac{\sigma_m}{\sigma_{eq}}\right) \tag{6}$$

Where,

$$\sigma_m = \frac{1}{3}(\sigma_1 + \sigma_2 + \sigma_3) \tag{7}$$

and

$$\sigma_{eq} = \frac{1}{\sqrt{2}}\sqrt{(\sigma_1 - \sigma_2)^2 + (\sigma_2 - \sigma_3)^2 + (\sigma_3 - \sigma_1)^2} \tag{8}$$

$$D = \int_0^{\epsilon_{eq}} \frac{d\epsilon_{eq}}{1.65\epsilon_0 \, exp\left(-\frac{3\sigma_m}{2\sigma_{eq}}\right)} \tag{9}$$

In Equation 6, the critical strain (ϵ_0) is the strain limit in a uniaxial tension test and represents a property of the material. Critical strain is measured from a true stress-strain curve generated by measuring the instantaneous diameter of a round specimen. Blade conducts the critical strain testing using a hydraulic load frame and vision system to track the minimum diameter of the tensile specimen during the test. Critical strain was measured for the material curves shown in Figure 37. The estimated critical strain for the base and weld material is 0.59. The curves in Figure 37 are a experimental measurement of true stress-strain data taken from the Blade material database and not estimated from the engineering stress-strain curve.

The materials' critical strain can be used in Equation 6, along with the outputs of an FEA, to determine the DFDI at various points within the model. A DFDI value of 1.0 represents the point at which a microcrack forms within a material. Values below 1.0 indicate that a crack has not formed. The DFDI approach was used with FEA to determine if a crack could initiate at the weld root during or just after the hydrotest.

5.4.2 Finite Element Analysis of Weld

An FE model of the weld was required for the strain-life and DFDI assessments. A finite element analysis of the Fort Ransom weld geometry was used to establish the following:

- In-service stress concentration factor at the root of the weld for the failed joint and for a typical weld
- Strain range at the failed weld root during a MOP cycle, after experiencing a hydrotest
- DFDI value for each load step
- Local stress state at the weld root for comparison with residual stress measurements of the pipe

The first step when developing the FE model was to establish the weld geometry at the failure location. Anderson extracted weld cross-sections from the U/S, D/S, and failed joints and measured the weld to compare against the 43rd edition of the API 5L standard. Table 10 is a summary of the Anderson measurements, including the plate offset edge, weld cap height, and out-of-line weld bead. Anderson concluded that all measurements met the API 5L 43rd edition specification.

Table 11 shows the angular measurements made by Anderson and Blade. Anderson measured the angle between the plate and a line tangent to the weld caps near the ID root radius and the angle between the ID surface of the plate on either side of the weld. Blade measured the angle between the OD surface of the plate on either side of the weld for comparison with the Anderson ID measurements and to assist with FEA geometry selection. The plate angular misalignment, known as peaking, is not directly limited by the API 5L standard or the TES-PIPE-SAW-US specification, but is covered by the flat spots and peaks requirement prescribed by 7.2.2 of the TES-PIPE-SAW-US specification, which states:

> The end of the pipe in the vicinity of the weld shall be checked with a template contoured to check for flat spots and peaks along both the ID and OD, to ensure a maximum deviation of no greater than 5/64" (2.0 mm), excluding any out-of-roundness…

The angular misalignment as measured at the ID ranged from (b)(4) for the failed joint, which is consistent with the Edinburg failure analysis, which found angular misalignment values of 13° and 15° on cross-sections extracted from the failed joint. According to the Berg Pipe inspection procedure BPP-SOP-MQC-002 [21] Section 5.15, an OD and ID template is used to measure the geometric deviations at the weld adjacent to the end of the pipe. The template is applied to the end of the pipe, and the deviation is measured using a taper gauge.

Figure 48 shows a schematic estimating the maximum misalignment angle permitted by the TES-PIPE-SAW-US specification using the ID gauge, given the allowable deviation of 5/64 in. (2 mm). The schematic indicates that the maximum misalignment angle at the ID is (b)(4) All but one of the values in Table 11 were below the estimated limit of 15.7°. The cross-section that failed the requirement had an angular misalignment of 15.9°, which is slightly above the limit. However, it should be noted that it is a reconstructed cross-section, meaning it is a fractured section that was put back together in the mount, which may cause errors in the measurement.

Based on the angular measurements in Table 11 and the understanding that geometric deviations were visually inspected and periodically measured, measurements were taken at the pipe ends, and that the limit was estimated from an idealized template, the failed joint met the TES-PIPE-SAW-US flat spot and peaks requirement in 7.2.2, which is consistent with the Edinburg failure.

Table 10: Weld geometric measurements from the Anderson report

Section Locations	Exterior		Interior		Out-of-Line[1] Weld Bead (mm)
	Radial Offset (mm)	Cap Height (mm)	Radial Offset (mm)	Cap Height (mm)	
U/S Joint (AA Fig. 57)	0.204	2.574	0.243	2.852	1.243
Intact Section (AA Fig. 58)	0.858	2.315	0.329	2.490	3.759
D/S Joint (AA Fig. 59)	0.281	3.048	0.255	2.068	0.155
Deepest Crack Depth (AA Fig. 60)	0.144	2.762	0.251	2.016	1.695
50% Crack Depth MET2 (AA Fig. 62)	0.217	2.869	0.168	2.321	2.349
Minimal Crack Depth, MET3 (AA Fig. 63)	N/A	N/A	0.101[2]	2.152[2]	2.360
25% Crack Depth, MET 4 (AA Fig. 64)	0.288[2]	0.975[2]	0.994[2]	1.873[2]	1.099[2]

Note 1: API 5L 43rd Edition only requires full penetration of the welds

Note 2: Mating of fracture surfaces and measurement may be impacted by the grinding of the weld cap and necking in the area

Table 11: Weld angular misalignment measurements

Joint	AA ID Plate Angle (deg)	AA ID Angular Misalignment (deg)	Blade OD Angular Misalignment (deg)
U/S Joint (AA Fig. 57)	173.4	6.6	8.7
Intact Section (AA Fig. 58)	167.7	12.3	12.0
D/S Joint (AA Fig. 59)	171.0	9.0	12.0
Deepest Crack Depth (AA Fig. 61)	166.5	13.5	13.4
50% Crack Depth MET-2 (AA Fig. 62)	166.5	13.5	-
Minimal Crack Depth, MET-3 (AA Fig. 63)	168.7	11.3	-
25% Crack Depth, MET-4 (AA Fig. 64)	164.1	15.9	12.8
Note 1: Mating of fracture surfaces and measurement may be impacted by the grinding of the weld cap and necking in the area			

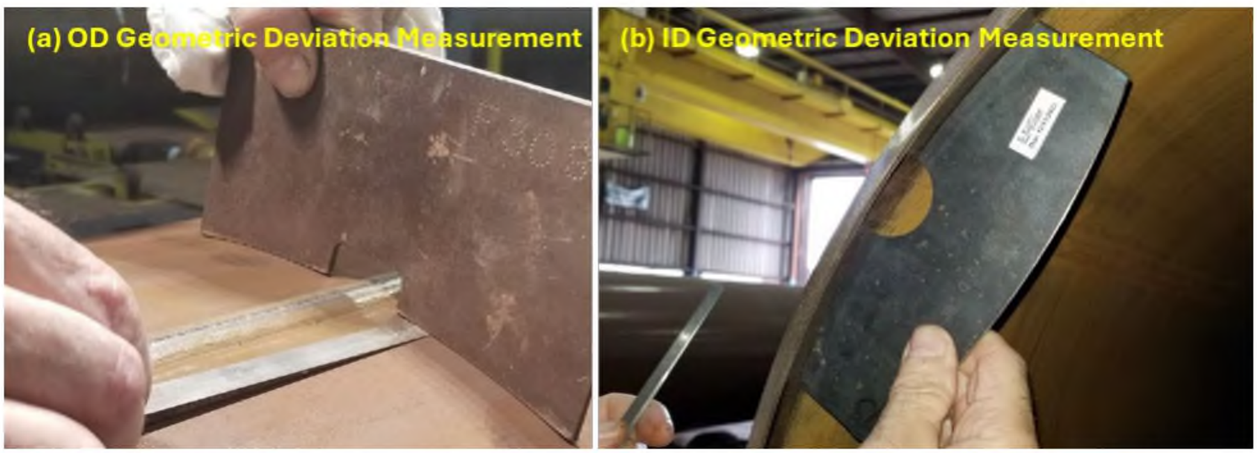

Figure 47: Method for measuring geometric deviations at the OD and ID surfaces [21]

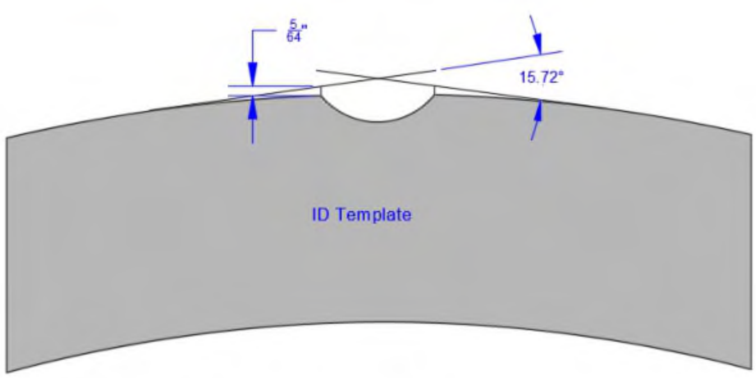

Figure 48: Angular misalignment limit based on ID template and TES-PIPE-SAW-US 7.2.2

Three FE models were created to assess the effects of weld root radius and angular misalignment. The Anderson cross-sections and corresponding measurements were reviewed, and two representative sections were selected for the FE model, shown in Figure 49 and Figure 50. Model 1 was an idealized DSAW weld with no angular misalignment, out-of-line weld bead, or plate offset edge. The exterior and interior weld cap heights were consistent with the failed joint. The purpose of Model 1 was to serve as a baseline for comparison with the failed joint geometry.

Models 2 and 3 were representative cross-sections taken from the Anderson report. Model 2 was scaled from the section shown in Figure 49, which was extracted from the failed joint upstream from the failure location. Model 3 was scaled from the section shown in Figure 50, which was a cross-section extracted through the middle of the fatigue crack at its deepest penetration. Note that the cross-section has been reconstructed since it is through a failed region. The OD toe and ID root radii were estimated as shown in Figure 51. The ID root radius was approximately 0.003 in. while the OD toe was 0.010 in. The weld root radius is challenging to determine from the micrographs and is an approximation.

Anderson found a corrosion pit at the internal weld root radius in one of the cross-sections. Figure 52 shows the images from the Anderson report with a radius measurement of the corrosion pit. The radius of curvature for the pit is approximately (b)(4) in., which is consistent with the ID root radius measurements. Since the actual root radius is challenging to measure and can vary along the joint length, two radii were considered for Models 2 and 3. A conservative value of (b)(4) in. was selected based on measurements, and a less conservative value of 0.010 in. was chosen based on the external weld value. Models 2a and 3a use a root radius of 0.003 in., and Models 2b and 3b use 0.010 in.

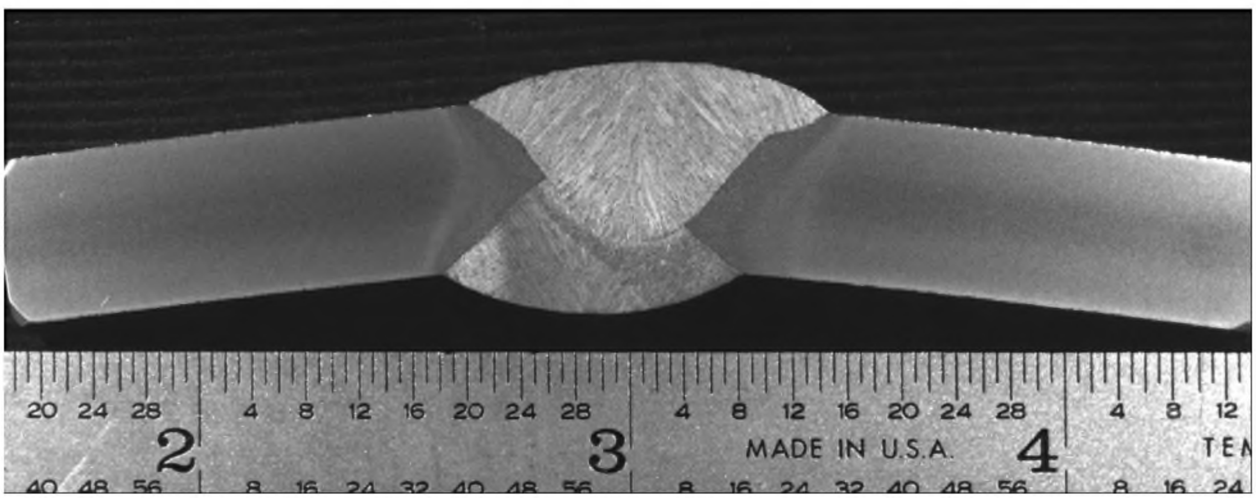

Figure 49: Model 2 - cross-section of seam weld through intact section of failed joint

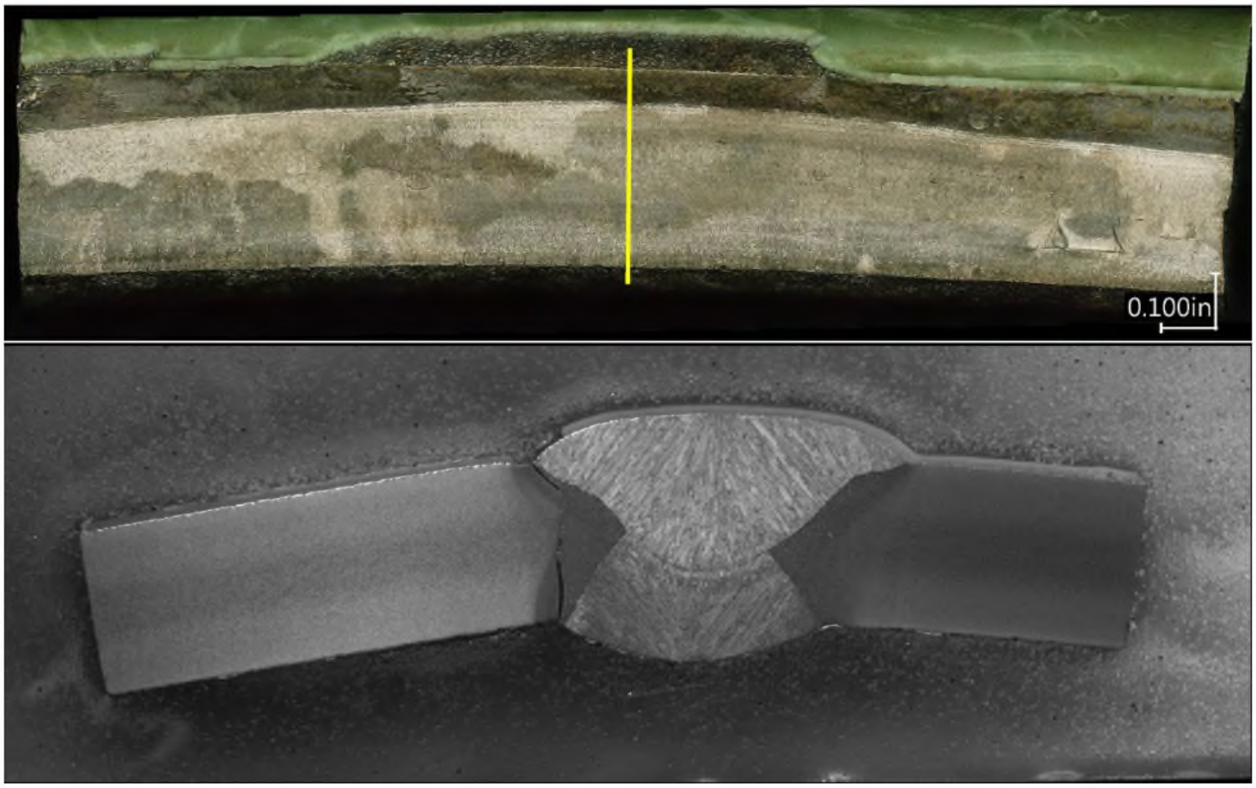

Figure 50: Model 3 - cross-section of seam weld through fatigue at deepest penetration

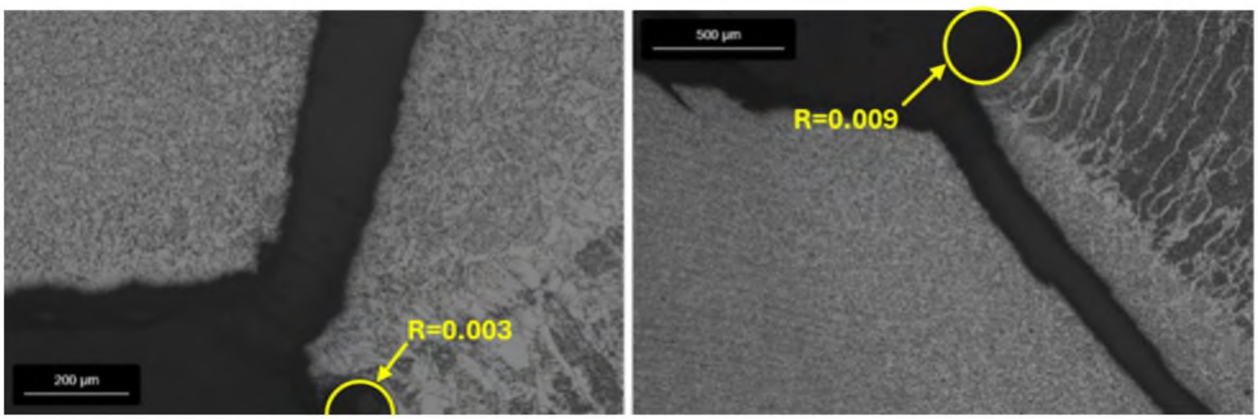

Figure 51: ID and OD toe radius estimation from Anderson cross-sections

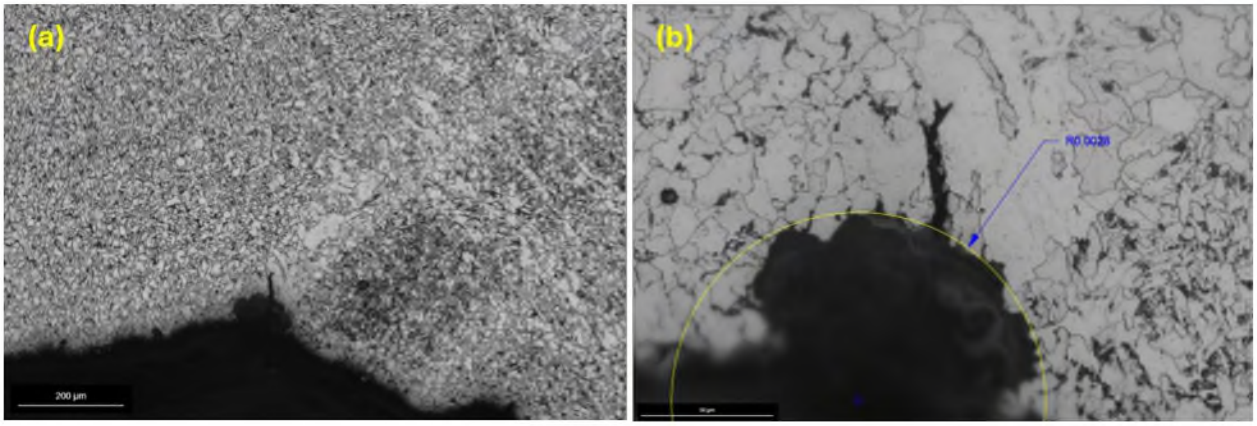

Figure 52: Corrosion pit with a crack at the weld ID root radius

Three materials were included in the model: base metal, HAZ, and weld. The base metal and weld true stress-strain data that were used for the Level 2 assessments are included in the 2D FEA. To establish the HAZ properties, the base metal curve was adjusted to meet the yield requirements and to account for the slightly softer HAZ. Figure 53, Figure 54, and Figure 55 show weld schematics for Models 1, 2, and 3.

The welds were modeled using plane strain elements (CPE4R). Figure 56 shows the geometry and weld mesh for all three models. The pipe was subjected to three load steps, consistent with the commissioning and service of the pipeline. The first load step was the hydrotest, which applied a maximum internal pressure of (b)(4) [redacted] kPa). Next, the internal pressure was lowered to 0 psi and then increased to the MOP, which was 1,440 psi (9,928 kPa).

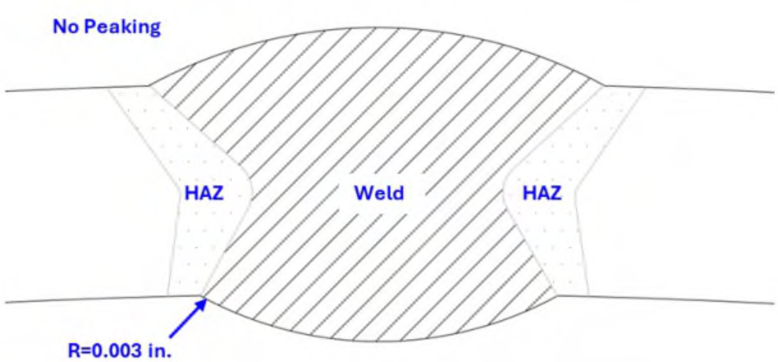

Figure 53: Model 1 FEA weld schematic

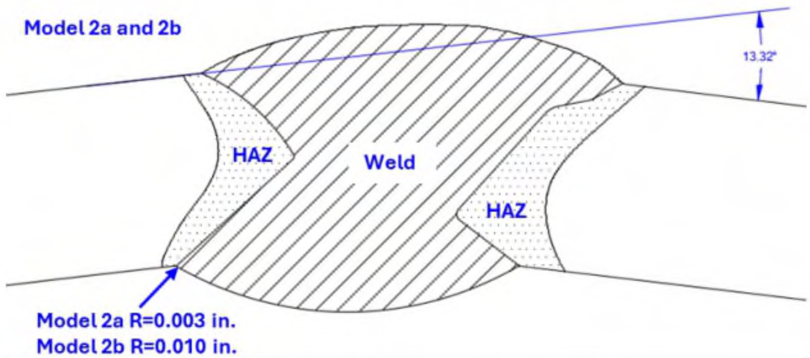

Figure 54: Model 2 FEA weld schematic

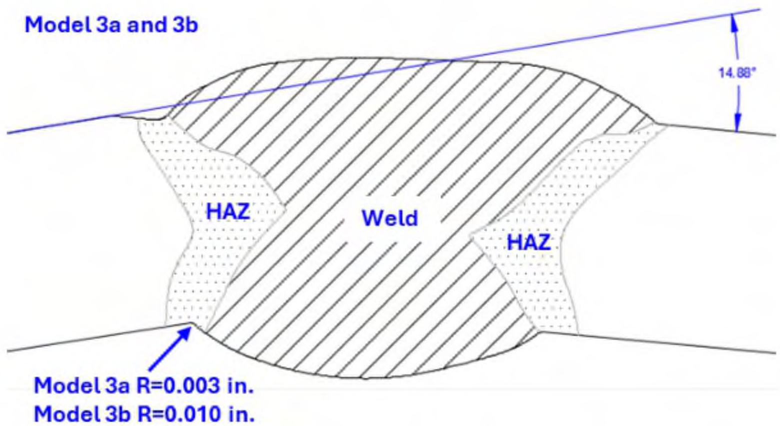

Figure 55: Model 3 FEA weld schematic

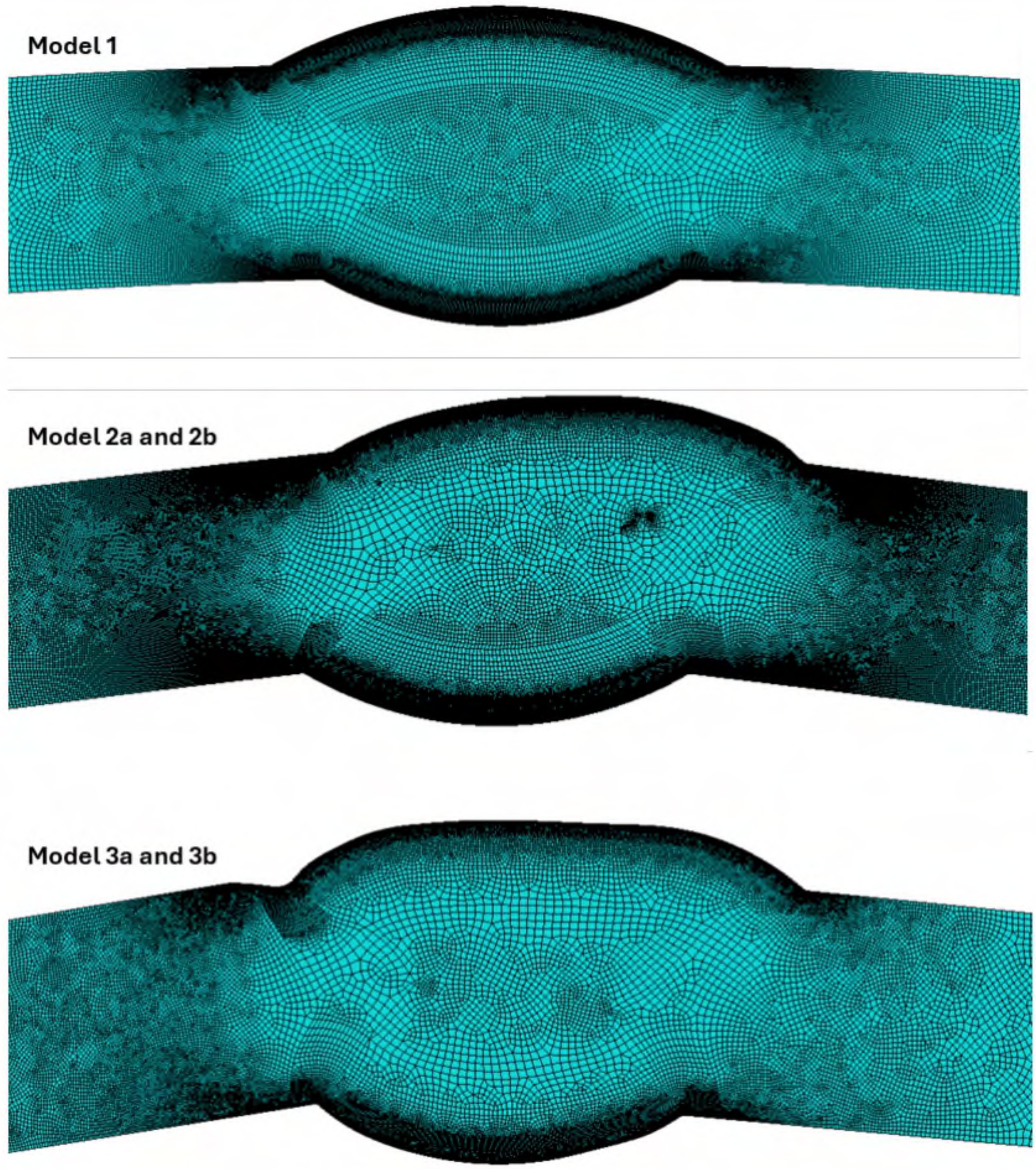

Figure 56: Geometry and mesh for models 1, 2, and 3

Table 12 shows a summary of the FEA results and includes the maximum principal stress, Von Mises stress, maximum principal strain, and DFDI for each load step of each model at the weld root radius. The results show that the angular misalignment significantly increased the stress at the internal root radius. The maximum principal stress for the ideal weld during the hydrostatic test is 109.6 ksi as compared to 165.5 ksi for the Model 3a geometry. The DFDI results indicate that, in general, a crack will not form at the internal weld root radius during or after the hydrotest. Model 3a is the only exception that achieved a DFDI value of 1.220 after releasing the pressure from the hydrostatic test. Note that the DFDI drops to 0.69 if the internal weld root radius is increased to 0.010, as was done in Model 3b.

Figure 57 shows a plot of SCF versus hoop stress normalized by SMYS. The plot shows that the SCF can range from approximately 3 to 9 at low pressures during a hydrotest, but will trend to approximately 2 at higher pressures due to local plasticity. CRES performed a similar assessment for the Edinburg failure, and their results are included for reference. The Blade results are consistent with CRES and show that the SCF is dependent on weld geometry.

Table 12: FEA results summary

Model	Load Setp	Max Principal Stress (ksi)	Von Mises Stress (ksi)	Max Principal Strain (in/in)	DFDI
Model 1	Hydro	109.6	86.4	0.0305	0.0709
Model 1	No Pressure	-11.2	87.8	0.0203	0.0837
Model 1	MOP	84.7	75.7	0.0262	0.0840
Model 2a	Hydro	161.4	131.6	0.2298	0.5568
Model 2a	No Pressure	-32.9	135.7	0.2003	0.7048
Model 2a	MOP	165.6	137.2	0.2158	0.7165
Model 2b	Hydro	139.5	117.2	0.1592	0.3370
Model 2b	No Pressure	-28.3	119.7	0.1383	0.4386
Model 2b	MOP	137.6	120.3	0.1502	0.4449
Model 3a	Hydro	165.5	202.9	0.3911	0.9509
Model 3a	No Pressure	-44.0	170.5	0.3575	1.220
Model 3a	MOP	171.8	208.7	0.3770	1.237
Model 3b	Hydro	134.5	157.8	0.2439	0.5127
Model 3b	No Pressure	-36.9	137.7	0.2189	0.6882
Model 3b	MOP	160.7	138.7	0.2336	0.6973

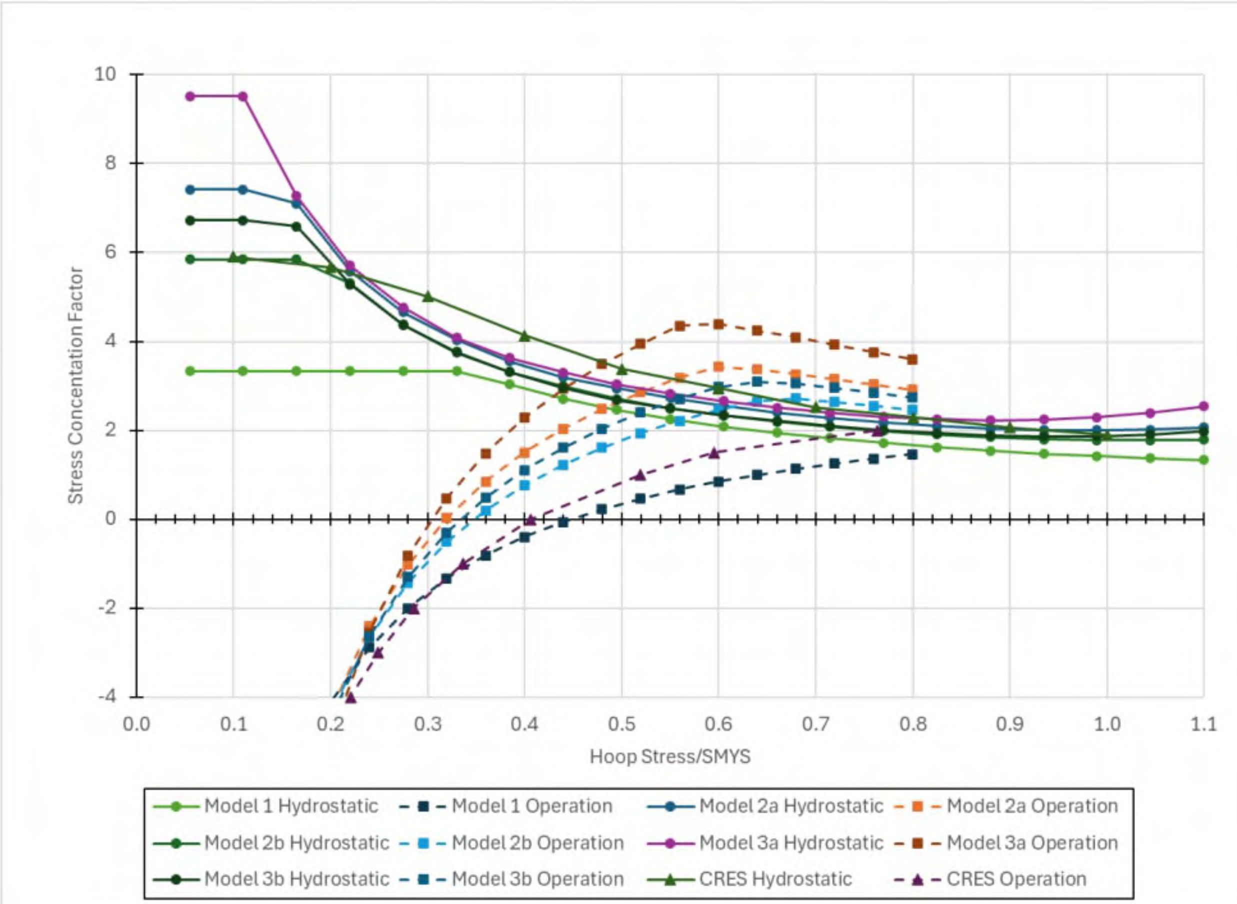

Figure 57: SCF versus percent SMYS

The Stress Concentration factor is high at the weld toe, especially in Models 2 and 3. The high SCF is at the ID surface in the weld toe region. It is a very important factor during crack initiation and is used in Section 5.4.3. However, once the crack initiates and propagates beyond the micro level to a macro level (approximately 1 to 2% of the wall thickness), the SCF is no longer relevant to the crack growth rate. The crack growth rate of macrocracks will be defined by the remote hoop stress, as specified according to Paris' law.

5.4.3 Strain-Life (SWT) Results

Table 13 shows the SWT inputs and resulting cycles to initiation for each model. The results show that the cycles to initiation vary depending on the model, with a minimum of 130 cycles (Model 3a) and a maximum of 1.13 × 10^10 (Model 1). Model 1 indicates that initiating a crack at the internal weld root of an ideal geometry is unlikely due to the operating pressure cycles. Models 2 and 3 indicate that a crack could initiate, but would require 130 to 478 MOP cycles.

Table 13: SWT initiation results

Model	Model 1	Model 2a	Model 2b	Model 3a	Model 3b
Weld Root Radius	0.003	0.003	0.010	0.003	0.010
Angular Misalignment	0	13.5	13.5	14.9	14.9
Strain Amplitude (in/in)	0.0076	0.0155	0.0119	0.0195	0.0147
Maximum Stress (psi)	84.7	165.6	137.6	171.8	160.7
Cycles to Initiation	1.13e10	207	478	130	240

5.5 Fatigue and Fracture Conclusions

A fatigue and fracture assessment of the failed joint was conducted to confirm the events leading to the rupture. First, the critical crack size was confirmed using the standard and material-specific API 579 Level 2 assessment. Then, a crack growth assessment was completed to determine the number of cycles needed to grow an initial crack to failure. Finally, DFDI and SWT were used to determine if a crack could initiate at the internal weld root within the number of equivalent cycles experienced by the failed pipe. The results from the analyses are as follows:

- A rainflow analysis of the SCADA data determined that the failed pipe section experienced 546 MOP cycles from 2010 to 2025.
- The critical crack length and depth were estimated to be 7.75 in. and 0.302 in. (78.2% NWT) based on stereo images from Anderson.
- An API 579 Level 2 material-specific analysis found that the crack length can range from 5.45 in. to 10.33 in., depending on the assumed toughness. The assessments indicate that the 7.75 in. length determined from the stereo images is a reasonable estimate for the critical crack length.
  - True stress-strain data for the X70 pipe material were selected from Blade's database.
  - Anderson fracture toughness values of 647 lbs/in, 1,175 lbs/in, and 1,471 lbs/in were considered.
  - For a 7.75 in. crack length, the estimated failure pressure was 1305 psi (less than 5% of actual)
- An API 579 Level 2 fatigue assessment found that a preexisting crack ranging from 12% to 36% is necessary to grow a 7.75 in. long crack to the critical crack depth within 15 years of operation.
  - This finding was consistent with fractographic evidence that indicated a difference in the fatigue striations beginning at a depth of 5%-10% from the ID surface.
  - The analysis suggests that additional cycles are needed if the crack initiates and grows to failure from operational loading only. Alternatively, a higher fatigue crack growth rate could achieve the same effect by reducing the time required for the crack to grow to failure. However, Blade did not find FCGRs for X70 that were higher than those found in API 579 or BS 7910.
  - The analysis assumes that the API 579 equations are sufficient for a crack at the internal weld root and that the microstructure achieves FCGRs consistent with standards. Blade found evidence that suggests the X70 HAZ can exhibit brittle behavior that could result in higher FCGRs, but could not find references providing the higher rates.

- RSI performed a transportation fatigue analysis that indicated a crack could initiate and grow at the weld root of abnormal seam weld geometry if at or near a contact point with the dunnage bearing strip. The RSI analysis also showed that the pipe body and ideal weld geometries are not susceptible.
- An API 579 Level 2 assessment was conducted to determine if tearing would occur to a pre-existing transportation crack during the hydrotest.
  - Anderson did not identify a tearing band on the fracture surface.
  - The analysis shows that tearing is unlikely to occur if the crack is close to the 12% depth.
- An FEA was conducted for an ideal weld and two cross-sections from the failed joint that experiences a hydrotest, followed by an MOP cycle to determine if a crack could initiate and grow to failure during operation only.
  - The analysis showed that the SCF during the hydrotest can reach values ranging from 3 to 9 at low pressures, but tends to approximately 2 at higher pressures because of local plasticity at the internal weld root.
  - The analysis is consistent with work conducted by CRES for the Edinburg failure.
  - The high SCF during the hydrotest creates a residual compressive stress at the ID weld root; the effect on initiation is accounted for, whereas it has no impact on FCGR.
    - The estimated initiation life includes the compressive stress in the applied principal strain amplitude.
    - The compressive stress is local to the ID weld root and does not influence the FCGR of a macro crack.
- A DFDI greater than 1.0 was achieved with Model 3a, which represented a worst-case weld geometry. A DFDI equal to or greater than 1.0 indicates the formation of a microcrack at the internal weld root.
  - The analysis shows that it is possible to initiate a crack with an abnormal weld geometry at the hydrostatic testing loads and subsequent MOP cycle. However, even if initiation occurs at or after the hydrotest, the pipeline does not experience enough damage from the operational pressure cycles to grow the crack to failure in 15 years. One needs an initial crack of around 12% to have failed in 2025.
  - RSI concluded that initiation during operation is possible due to the high SCF values at the weld toe. This observation is consistent with the DFDI value, but initiation and growth during operation is unlikely due to the number of MOP cycles and failure occurring in 15 years.
- Blade determined the estimated initiation life using the SWT model and found that initiation from pressure cycles is possible in 130 to 478 cycles.
  - The initiation cycles reduce the available years for growth by 3.4 to 12.6 years.
  - Decreasing the available years for crack growth only increases the required preexisting crack size, making it unlikely that initiation and growth to failure only occurred during operation.
- The crack depth as a function of year was estimated using the yearly SCADA data and an API 579 Level 2 fatigue analysis. The results indicate that the crack would have had an estimated depth of 30-50% during the 2020 (b)(4) run, assuming a 12% preexisting crack.

6 Control Room Response, Leak Detection, and Emergency Response

A review of South Bow's response to this incident was performed to determine if their actions, or potentially lack thereof, may have contributed to the estimated release volume of 3500 barrels (bbl) of crude oil [22] after the rupture occurred.

A root cause approach was used, as represented graphically in Figure 58 below.

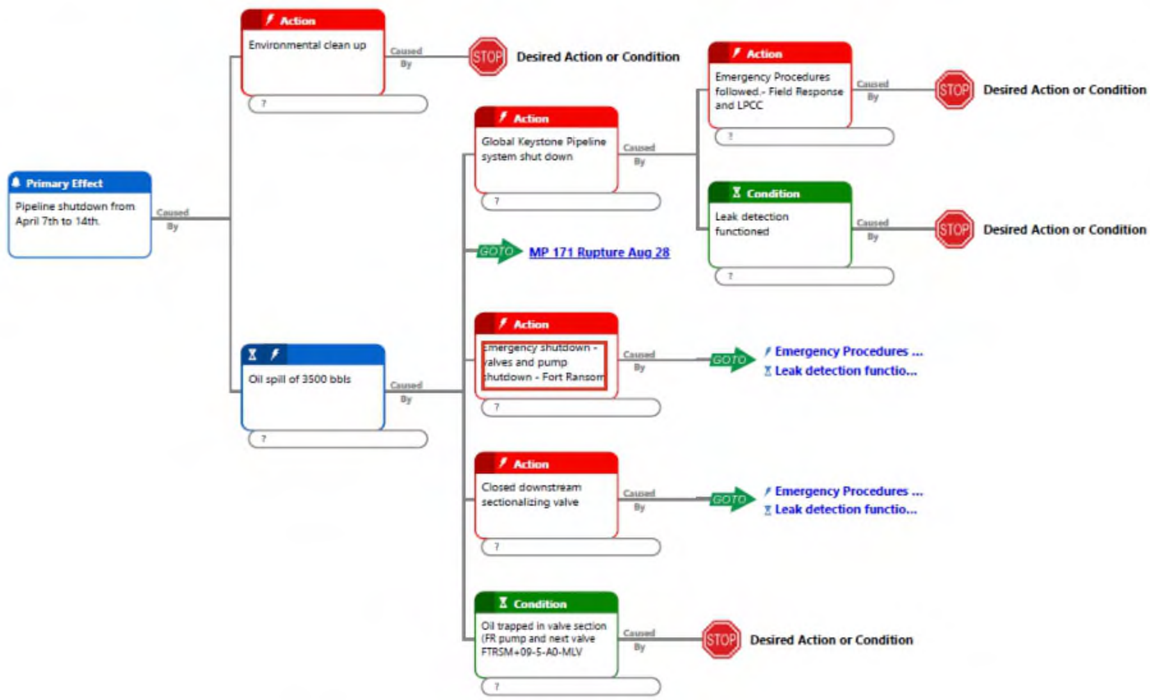

Figure 58: Root cause for emergency response

The following sections detail the Control Room response, Leak Detection System (LDS) performance, and Emergency Response activities.

Overall, no deficiencies were noted or recommendations made regarding South Bow's actions. The response of the Control Room and field responders resulted in pipeline shutdown initiation in a little over [redacted] with complete isolation of the failed section within approximately [redacted] of the rupture which minimized the release. This is faster than the average pipeline shutdown time of approximately [redacted] and an average isolation time of approximately [redacted] as calculated for crude oil pipeline incidents using PHMSA data [23]. Records within this data that were incomplete or appeared to be erroneous were not used in the calculations. Field response teams mobilized resources in a timely manner to contain the spill and minimize its spread.

6.1 Control Room Response

The operation of this pipeline is managed remotely from South Bow's Liquid Pipeline Control Centre (LPCC) in Calgary, Alberta, and South Bow's Backup Control Center (BCC) in Airdrie, Alberta. The LPCC provides 24 x 7 monitoring and control of all Liquid Pipeline facilities.

On April 8, 2025, the day of the rupture, a maintenance day was planned on the Keystone pipeline. In preparation for this, a throughput rate reduction was initiated at several pump stations at 4:00 am MST. This is shown graphically in Figure 59 at the FTRSM Pump Station by a decrease in the flow rate starting shortly after [redacted], accompanied by corresponding changes in station suction and discharge pressure.

[redacted]

Figure 59: Fort Ransom pump station flowrate (blue line), suction pressure (orange line), and discharge pressure (green line)

Station flow stabilized shortly after [redacted] and remained so until the time of the rupture at approximately [redacted] Discharge pressure, which represents the pressure at the rupture location, was initially [redacted] psig before the rate reduction and increased to [redacted] psig after flow stabilization, before dropping due to the rupture.

A review of the SCADA alarm logs on April 8th, near the time of failure, shows a Station Suction Pressure Low alarm at the FTRSM Pump Station at [redacted]. This coincided with several station alarms as the station controls responded to the increase in flow rate and the drop in pressure associated with the rupture downstream of the station. These changes in pressure and flow rate are illustrated graphically in Figure 53.

At [redacted] the Leak Detection System (LDS) identified a loss of flow between FTRSM and Ludden Pump Station (LUDDE), which crossed the [redacted], and at [redacted] MST, a shortage alarm (FTRSM-A0-STATELEAK) was generated by LDS.

Maintenance personnel at FTRSM initiated an on-site Emergency Shutdown (ESD) at [redacted] MST. This terminated the flow through the pump station and isolated it from the upstream and downstream pipeline sections. The LPCC was contacted by onsite personnel at 05:43:24 to confirm that the pipeline was leaking

Based on the information received by the LPCC (i.e., pressure drop, leak alarm, phone call, flow rate data, etc.), the pipeline was tripped at 5:43:35. The LPCC sectionalized and isolated the pipeline, including the impacted FTRSM segment, using and in-house developed SCADA application in conjunction with LPCC procedures. The rupture section was fully isolated by 05:50:32 am MST after accounting for valve closure times.

It was noted during communications with LPCC personnel that field confirmation of a leak, as occurred in this incident, was not required for the controller to initiate a system shutdown. Current LPCC procedures [24] were reviewed and indicate that [redacted] an emergency pipeline shutdown is performed.

The LPCC made internal notifications to the First Responder, Regional EOC, US Regulatory Compliance, Canadian Regulatory Compliance, Oil Scheduling, and Operations Engineering between 5:48 a.m. and 6:19 a.m. MST. The Regional EOC call was initiated at approximately 6:20 a.m. MST (8:20 a.m. CDT) to provide an update on the current situation with the leak and to coordinate emergency response activities.

Based on the SCADA timeline and actions taken by the LPCC and field response, the pipeline was shut down in a timely manner in response to the rupture. Sectionalization was initiated within [redacted] and [redacted] of the initial pressure drop, and complete isolation of the failed segment was achieved within [redacted] after the rupture occurred.

6.2 Leak Detection System (LDS)

6.2.1 LDS Description

South Bow takes an overlapping and layered approach to pipeline leak detection and utilize both periodic and continuous systems:

Description of Periodic Pipeline Leak Detection Layers:

- Right of Way Patrols: Inspection of the right-of-way for signs of leaks or other hazards and managed as part of the Pipeline Integrity Program. These patrols are conducted at least [redacted] and are conducted at intervals not exceeding [redacted] The last patrol conducted on the ruptured segment was on April 5, 2025, via aerial patrol. No leak observations were noted.
- Inline Inspection Tools: In-Line inspection (ILI) smart tools that traverse the length of a pipeline to collect data and monitor its condition are utilized based on risk assessment for the detection of leaks. The last ILI leak detection tool run on the segment that ruptured was performed on February 13, 2024, using a Pipelines2Data (P2D) acoustic leak detection tool. There were no reported indications of a leak.
- Public Awareness Program: The public awareness program, managed by the Land & Public Awareness team at South Bow, educates the public about pipeline safety, potential hazards, and how to recognize and report potential leaks.

Description of Continuous (real time) Pipeline Leak Detection Layers:

- 24/7 Control Room Monitoring

Pipeline is monitored by the Control Centre 24 hours per day, 7 days per week (24/7) for abnormal operating conditions. The Controller may use independent data (for example the output of one of the other leak detection systems) and/or other information (such as valve or pump status values) in the analysis of the line for leaks.

- Shut-In Leak Detection (Pressure Monitoring)

  Pressure monitoring is used during shut-in periods for leak detection. In addition to the automated Shut-In Leak Detection application, the 24/7 Control Room monitoring can watch for unexpected drops in pressure during these shut in periods. The last shut-in period for this section occurred on April 2, 2025, between 11:15 and 12:15 PM, and no leak was detected by LDS.

- Standard Computational Pipeline Monitor (CPM)

  Standard CPM Methods include Line Balance, Volume Balance and Modified Volume Balance. This software-based CPM system is part of the SCADA vendor's Liquid Management System (LMS) suite of applications. The PLM module within LMS performs a standard volume balance at set time intervals and will alarm when volume balance limits are exceeded. This system serves as a redundant method for real-time leak detection on the mainline pipe.

- Advanced Computational Pipeline Monitor (CPM) - RTTM

  This leak detection system is based on a real-time transient model and utilizes AVEVA's SimSuite 6.7.2.774 Pipeline Real Time Transient Model (RTTM). This advanced volume balance CPM-based leak detection system is the most sophisticated application available in the control room.

6.2.2 LDS Performance

Based on the findings of the metallurgical report [17] the crack that failed was not leaking prior to failure. The report states "There was no evidence observed that the fatigue crack penetrated the full wall thickness, indicating the final overload and subsequent petroleum release was an instantaneous event that occurred when the remaining ligament could no longer support the applied load." This meant that only the continuous control room monitoring and computational pipeline monitoring layers could have effectively detected the leak on a timely basis.

A review of the CPM based leak detection system (LDS) in the hours leading up to the rupture indicated that the primary and backup CPM servers and SCADA real-time systems were running with full redundancy. Additionally, the Key Performance Indicators indicated that the LDS was operating within expected parameters and that the associated field equipment was operating within specifications.

The leak detection thresholds for the Keystone system are:

- [redacted]
-
-
-

At the time of the rupture the flowrate was approximately [redacted] m^3/hr.

The first indication in the SCADA alarm log of a potential leak was at [redacted] when the suction and discharge pressure at Fort Ransom Pump Station dropped. The LDS crossed the [redacted] integration period threshold at [redacted] and a leak section alarm was generated at 05:42:45 MST. An ESD was initiated at the pump station at [redacted]

There were no indications of a leak in LDS before the rupture, and the metallurgical evaluation of the failed pipe validated this. The CPM system functioned as intended, generating a leak alarm within [redacted] of the first indications of a leak. This was 17 seconds before the ESD initiation at the pump station by onsite field personnel. The leak alarm and confirmation of a rupture by onsite personnel enabled a rapid response by Control Center personnel, who shut down the pipeline and isolated the failed section.

6.3 Emergency Response

As mentioned, the day of the rupture was a planned maintenance day on the Keystone pipeline. As part of this plan, South Bow maintenance personnel began arriving at the FTRSM Pump Station at approximately 6:40 am CDT (local time) (4:40 am MST) to work on unit 4 pump. At 6:43 am CDT, an onsite Technician called LPCC to check in and take Unit 4 into local control. At approximately 7:40 am CDT, the Technician reported that he was working on the outboard of Unit 4 pump, and the piping started to shake due to activation of a control valve. This was accompanied by a loud bang originating nearby. The Technician recognized this as a potential leak and ran to the front gate, activating the station (ESD) button at approximately 7:42 am CDT (ESD was recorded in SCADA at 05:43:02 am MST). Another Technician on their way into the Fort Ransom Station placed a call to LPCC at approximately 07:48 am CDT, informing them of the leak and instructing them to shut down the pipeline immediately. The pipeline segment containing the rupture from FTRSM Pump Station to the next downstream MLV (FTRSM+09-5-A0-MLV) was fully isolated by approximately 07:50 am CDT (recorded by SCADA at [redacted]. The Company First Responder arrived on-site at approximately 08:00 am CDT to assess the situation. The rupture was visually confirmed by the observation of oil coming from the ground approximately 550 yards south of the FTRSM pump station.

As stated in the Incident Action Plan [25] once the pipeline was isolated, the primary incident objectives were to:

- Ensure the Safety of the Public and Response Personnel
- Maintain isolation of the source of the discharge
- Contain and recover spilled material and contaminated soil
- Maximize protection of environmentally sensitive areas
- Keep interested parties informed of response activities
- Manage a coordinated response effort

Initial actions on April 8, 2025 (Day 1) consisted of communicating the status of the incident to internal and external stakeholders, securing the incident site to ensure the safety of the public and response personnel, ensuring isolation of the failed segment, mobilizing emergency response contractors and resources, and standing up Incident Command.

To secure the area around the release location a number of road blocks and 3 security checkpoints were used to establish a perimeter and restrict access. A roving patrol was also used for both day and night shifts. A Temporary Flight Restriction was established within a 2 mile radius around the release location up to an elevation of 2,500 ft. Air monitoring was established to monitor benzene levels at local residences and in work areas. An emergency line locate was called into 811 and berms were constructed to contain the crude oil outflow.

Incident response crews were mobilized to initiate spill containment and recovery and repair activities. It was determined that one stopple would be required approximately 480 ft downstream of the rupture to isolate the ruptured pipe and permit product drain down and pipe cut-out and replacement. The valves at the FTRSM Pump Station, approximately 550 yards upstream of the rupture, provided adequate isolation, and it was determined that an upstream stopple was not required. Equipment matting was mobilized to facilitate construction of access roads into the site. Stopple equipment including split tees were mobilized from Tulsa, OK. Welders were mobilized from various job sites in the U.S. Representatives from PHMSA arrived onsite to monitor response and failure investigation activities.

On April 9, 2025 (Day 2), access was gained to the stopple location, and excavation for installation of the stopple was initiated. Oil recovery operations started in the southeast collection area as well as at the feature location. It was noted that oil was vacuumed 2 ft down at the feature location, and the oil level remained down, indicating that oil outflow from the feature had stabilized by that point.

Initial exposure of the rupture feature occurred on April 10, 2025 (Day 3) and stopple location excavation was completed. Welding of the split tee for the stopple was completed on April 11, 2025 (Day 4) and the stopple was set into the pipe on April 12, 2025 (Day 5). Replacement pipe joint (60 ft) pressure testing was completed.

On April 13, 2025 (Day 6), the drain-down and removal of the pipe segment containing the feature were completed. The pipe containing the rupture feature was released from the site on April 16, 2025, and arrived at Anderson and Associates on April 17, 2025. The pre-tested replacement pipe was welded into the line, and NDE was completed. PHMSA approved the restart plan.

The line was restarted on April 14, 2025 (Day 7), and the Incident Management Team (IMT) was stood down at 7:00 p.m. CDT on April 15, 2025 (Day 8).

The spill extents are shown within the bermed areas in Figure 60 and Figure 61. A release volume of 3500 barrels (bbl) of crude oil was estimated [22]. The closest High Consequence Area (HCA) is located approximately 3,800 ft south and the closest Contributory Pipeline Segment (CPS) is approximately 1,776 ft downstream (south) of the rupture location. The rupture was not located within a CPS that could affect an HCA.

(b)(7)(F); (b)(3):49 U.S.C. § 60138

[redacted]

Figure 60: Spill extents (crude oil pooling shown in black)

Figure 61: Spill extents – aerial photo of spill

In evaluating the response to this incident, South Bow's internal guidelines as well as the RCFA findings related to the previous incident response were reviewed to determine if any actions could have minimized the release of crude oil during this incident. South Bow has included the following general guidelines in its Emergency Response Plan [26].

Table 14: Keystone Pipeline System Response Time Standard

Phase	Response Time Standard	Actions	Description
Phase 1	Initiated immediately upon recognition of a pipeline emergency	Pipeline Shutdown Isolation	The remote shutdown of the pipeline through a control center should be undertaken immediately upon recognition of an emergency. Conduct notification to local personnel to initiate manual closures of valves.
Phase 2	2 Hours	Emergency Response Activities	The structuring of an emergency response management system should be undertaken immediately upon recognition of an emergency. The establishment of the Incident Command System should occur in no more than two hours. This can be through the establishment of an Incident Commander, preparation of the ICS 201 Form or other ICS driven activity.
Phase 3	3 Hours	Staff on-site	Company First Responder on scene within 3 hours, weather permitting safe travel to location.
Phase 4	6 Hours	Initial Emergency Response Equipment on-site	Initial response equipment should be on-site within 6 hours of recognizing an emergency, with additional supporting requirements taking no more than 72 hours. This can be achieved with in-house, mutual aid, spill cooperatives or contracted response equipment. Emergency Response equipment is based on a calculated formula that determines worst-case discharge amounts, which, in turn, determine the planned quantity of equipment for response.

As noted above the pipeline was shut down and the segment of pipe containing the failure was isolated (Phase 1) within [redacted] of the first indication of a rupture. An Incident Commander arrived onsite at 07:59 am CDT, approximately 17 minutes after the rupture (Phase 2). Company personnel were at the FTRSM Pump Station when the rupture occurred and they along with the Incident Commander responded to the scene of the failure within approximately 18 minutes (Phase 3). The first response equipment consisted of the response trailer which contained spill containment resources which were used to construct berms to contain the surface flow of oil. This trailer arrived onsite at 10:42 am CDT, approximately 3 hours after the rupture (Phase 4). These response timelines met South Bow's internal guidelines.

Subsequent to the previous Keystone pipeline release on October 29, 2019 at Edinburg +0.2 an RCFA was performed [27] which identified a potential improvement regarding enhanced availability of contractors and logistical support for stopple installation. This was based on what was perceived as a one day delay due to initiation of stopple equipment on Day 2 of that incident as well as the two-day mobilization timeline of the selected stopple contractor which resulted in the stopple being set on Day 6. In this incident South Bow personnel stated that the request to mobilize stopple equipment and support personnel was initiated on Day 1 with the welders being the last to arrive on Day 4. This resulted in the stopple being set on Day 5. While there is still potential room for improvement in this timeline South Bow did improve the stopple timeline by 1 day compared to the previous incident. In this particular scenario, based on the observation that the outflow of oil from the rupture location had stabilized by Day 2 it is unlikely that expediting stopple installation would have had an impact on minimization of the release.